*fractal and fractional*

MDPI

*Review*

# Multifractality in Complex Systems: From Scaling Structure and Long-Range Organization to Learning Systems

**Enrico De Santis [1], Alessio Martino [2,*] and Antonello Rizzi [1]**

[1] Department of Information Engineering, Electronics and Telecommunications, Sapienza University of Rome, Via Eudossiana 18, 00184 Rome, Italy; enrico.desantis@uniroma1.it (E.D.S.); antonello.rizzi@uniroma1.it (A.R.)
[2] Department of AI, Data and Decision Sciences, Luiss University of Rome, Viale Romania 32, 00197 Rome, Italy
* Correspondence: amartino@luiss.it

**Abstract**

Multifractal analysis has evolved from a formalism for heterogeneous scaling into a broader framework for investigating structure, dynamics, representation, computation, and learning systems. This critical integrative review synthesizes methodological foundations, evidence criteria, complex-system applications, network methods, computational uses, and multifractal analyses of learning systems. Particular attention is given to apparent versus supported multifractality and to finite size, temporal correlations, heavy-tailed distributions, estimator choices, surrogate testing, and mechanistic interpretation. To compare heterogeneous studies, we organize the literature through a three-dimensional framework in which locus identifies where multifractality is measured, role specifies how the resulting quantities are used, and evidence characterizes the support for their interpretation. The framework clarifies how multifractal information functions across description, diagnosis, representation, adaptive computation, trainable operators, and the analysis of learning systems. We further distinguish complexity in data, models, input-conditioned hidden representations, and outputs, identifying direct multifractal analysis of hidden representations as comparatively underexplored. Across domains, multifractal claims are treated as object-dependent and tied to the support, measure, scale, and estimator used to construct the analyzed object. Future progress will depend on stronger finite-size controls, cross-method comparability, causal validation, and explicit definitions of analytical objects.

**Keywords:** multifractal analysis; complex systems; scaling; long-range dependence; complex networks; machine learning; deep learning; artificial intelligence

Check for updates

Academic Editor: António Lopes

Received: 1 October 2026
Revised: 21 October 2026
Accepted: 23 October 2026
Published: 26 October 2026

**Copyright:** © 2026 by the authors. Licensee MDPI, Basel, Switzerland. This article is an open access article distributed under the terms and conditions of the Creative Commons Attribution (CC BY) license.

## 1. Introduction

Complex systems often exhibit fluctuations and structures whose scaling behavior cannot be summarized by a single exponent. Local regularity may vary across positions, timescales, or dynamical regimes, so the relevant question concerns how scaling heterogeneity is distributed and what that heterogeneity reveals about the process that generated it. The multifractal formalism was developed precisely to address this problem by replacing a single global dimension with a spectrum of local scaling exponents and their associated dimensions [1–4]. This shift provided a language for characterizing intermittent measures and singular structures and later enabled analogous analyses of nonstationary time series, particularly through MultiFractal Detrended Fluctuation Analysis (MF-DFA) [5].

The scientific use of multifractality has broadened considerably since these foundations were established. In turbulence and physiological dynamics, multifractal spectra have been

used to describe heterogeneous organization across scales and to relate that organization to intermittency, regulation, and long-range dependence [6,7]. In financial systems, a large body of work has examined how temporal correlations and heavy-tailed fluctuations contribute to the observed spectrum and how these contributions affect its interpretation [8]. Research on complex networks has extended fractal and multifractal analysis to graph-structured supports, where distance, neighborhood construction, and the definition of mass become explicit modeling choices [9]. More recently, multifractal quantities have entered machine learning pipelines as compact representations [10,11], adaptive control variables [12,13], and trainable components [14], while contemporary work has revisited learning systems themselves as multiscale objects through loss landscapes and neuron-interaction networks [15,16]. This direction also has earlier antecedents in the statistical mechanics of learning, where random input patterns were shown to induce multifractal partitions of perceptron and feedforward-network coupling spaces [17,18].

As the scientific scope of multifractality has expanded, the same terminology has come to describe scientific operations that differ substantially in purpose. A broad singularity spectrum can serve as a descriptor of heterogeneous scaling, as evidence supporting a dynamical interpretation, as a feature vector for pattern recognition, as a variable that modulates a model, or as a property attributed to the model itself. These uses cannot be evaluated through a single interpretive template because they refer to different supports, measures, scales, and evidential requirements. The problem is intensified by the fact that finite-size effects, distributional heterogeneity, temporal correlations, detrending choices, and estimator-specific assumptions can all influence the width and shape of the inferred spectrum. Recent methodological work has sharpened the distinction between detecting broad multifractal signatures and establishing the conditions under which those signatures support stronger structural or mechanistic claims [19–21].

The emergence of learning systems adds a further layer to this problem because the object of analysis can now be produced by the learning process itself. Multifractal structure may be sought in the training data, in the geometry of a model, in an interaction network derived from its units, in the trajectory of internal representations induced by a particular input, or in the generated output. These loci are connected by computation, yet they remain mathematically distinct. A spectrum estimated from generated text, for example, characterizes the organization of the output sequence and does not by itself identify the scaling structure of the hidden representations that produced it. Likewise, a multifractal loss landscape describes a property of parameter-space organization whose relation to input-conditioned computation requires an additional inferential step. This separation motivates a review architecture capable of following multifractality across changing objects without treating those objects as interchangeable. It also keeps the interpretation of each spectrum tied to the scientific object from which that spectrum is constructed.

Existing reviews provide strong foundations for several parts of this landscape. Methodological surveys compare the principal formalisms and estimators used to recover multifractal spectra [22], while domain-specific reviews synthesize extensive literatures in medical imaging, finance, hydro-climatology, and network geometry [8,23–25]. The growing interaction between multifractal analysis, network science, and machine learning motivates a complementary synthesis organized around the changing scientific role of multifractal information. The aim of this review is to examine how multifractality has been used across complex systems, how the evidential basis of multifractal claims varies with the object under study, and how recent developments in learning systems extend the locus of analysis from observed data toward computational organization.

To support this synthesis, we use a three-dimensional framework. The *locus* identifies the scientific object on which multifractality is measured, spanning temporal signals, spatial

structures, networks, symbolic sequences, and learning systems. The *role* describes what the resulting quantities contribute to the analysis, from description and diagnosis to representation, adaptive computation, and endogenous model organization. The *evidence* dimension records the support available for interpretation through scaling stability, uncertainty analysis, surrogate-based source discrimination, finite-size assessment, cross-method validation, and mechanistic arguments. Section 10 formalizes these coordinates and uses them to compare studies whose mathematical objects and scientific objectives would otherwise remain difficult to place within a common account.

Figure 1 provides a compact map of the conceptual trajectory followed in this review. The upper panels summarizes the expanding scientific roles that multifractal analysis may assume across different classes of problems, whereas the lower panel introduces the Locus–Role–Evidence coordinates used throughout the paper to compare heterogeneous contributions within a common analytical framework. The figure is intended as a reading guide rather than as a rigid taxonomy.

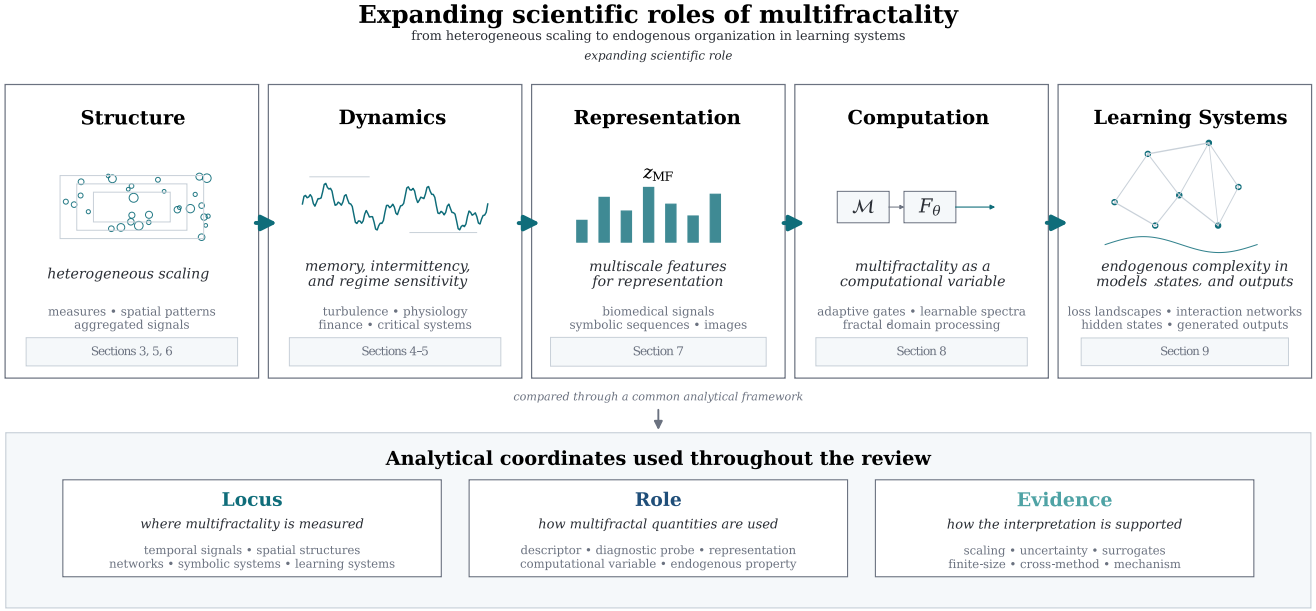


**Figure 1.** Conceptual map of the expanding scientific roles of multifractality across the areas considered in this review. The upper sequence summarizes a progression from structural description and dynamical interpretation to representation, computation, and learning systems, thereby reflecting the widening functions that multifractal analysis can assume in complex system research. The lower row introduces the three analytical coordinates used throughout the review.

This review follows this conceptual trajectory and is organized as follows: Section 2 describes the review design and the construction of the literature corpus, and Section 3 introduces the minimum common formalism required for subsequent comparisons. Section 4 examines the distinction between apparent and supported multifractality and develops the evidence dimensions used later in the paper. Sections 5 and 6 consider multifractality as a probe of structure, memory, dynamics, spatial organization, and network topology. Sections 7 and 8 examine the transition from multifractal signatures as external representations to multifractal quantities that participate directly in learning algorithms. Section 9 then reverses the direction of analysis by treating learning systems as multifractal objects. The final framework in Section 10 integrates these strands and identifies research directions that follow from their comparison. Section 11 concludes the paper.

## 2. Review Strategy and Literature Corpus

This study adopts a critical integrative review design aimed at reconstructing the conceptual and methodological development of multifractal analysis across different classes of complex systems and comparing the scientific roles assigned to multifractal quantities. The literature search was designed to identify foundational contributions, methodological advances, representative empirical applications, critical studies of multifractal inference, and recent work at the interface with machine learning and artificial intelligence. The search was not intended to enumerate every domain in which a multifractal estimator has been applied.

The corpus was assembled through iterative searches of scholarly bibliographic services and publisher platforms, complemented by backward and forward citation tracing from foundational and review articles. The temporal coverage extends from the mathematical development of the multifractal formalism in the 1980s up to September 2026. Particular attention was given to work published from 2020 onward in complex networks, computational uses of multifractal quantities, deep learning, and large-model analysis. Foundational papers were retained when they introduced concepts or estimators required to interpret later developments, while recent papers were prioritized when they modified current understanding of multifractal evidence or extended the locus of analysis to new computational objects.

The search strategy combined terms from the literature on multifractal formalisms and estimators with terms concerning source attribution and validation, applications to complex systems and networks, and computational uses in machine learning or artificial intelligence. Representative queries included combinations of "multifractal analysis", "MF-DFA", "singularity spectrum", "multifractal network", "spurious multifractality", "finite-size multifractality", "surrogate multifractal", "multifractal feature", "multifractal machine learning", "multifractal neural network", "loss landscape", and "large model". Searches for neural representations also included neighboring concepts such as intrinsic dimension and representation geometry when they were needed to delimit multifractality from adjacent forms of multiscale or geometric analysis.

Peer-reviewed journal articles and established conference proceedings were prioritized throughout corpus construction. Preprints were considered only when a definitive peer-reviewed version was unavailable and the work was necessary to characterize a rapidly developing frontier, with such cases identified explicitly when present. Application papers were included when they contributed methodological insight, represented a scientifically important use of multifractality, or illustrated a transition in the role of multifractal information. Repetitive applications that reported a spectrum without substantial methodological validation or conceptual contribution were not prioritized. Self-citations were restricted to already published contributions with stable bibliographic records.

Bibliographic metadata were checked against publisher or proceedings records whenever possible, with preference given to the definitive version of each work. Citation chaining was used to recover earlier methodological contributions that remained conceptually relevant even when later applications cited them only indirectly. Recent frontier papers were retained when they introduced a new locus, a new computational use of multifractality, or a methodological result capable of changing the interpretation of previous evidence.

Where inferential distinctions benefit from direct visualization, the review also uses controlled synthetic calculations as explanatory benchmarks. These calculations are reported separately from the literature corpus and are not treated as independent empirical evidence for any application domain.

The literature was then organized according to the framework developed in Section 10. Each contribution was classified by the locus of multifractal analysis, the role assigned to

multifractal information, and the forms of evidence used to support interpretation. This procedure provides a transparent basis for comparison while preserving the character of the study as a critical integrative review. The resulting corpus is intended to be conceptually representative of the field and sufficiently broad to support cross-domain synthesis, while avoiding a claim of exhaustive coverage that would require a systematic-review protocol.

## 3. Multifractal Formalism: A Common Language

Multifractal analysis extends ordinary fractal characterization by resolving how scaling behavior is distributed across a heterogeneous support. A single fractal dimension summarizes the rate at which an object or measure fills space under a change of scale, whereas a multifractal description retains the variation in local scaling exponents and relates that variation to subsets of the support. The resulting formalism provides a common mathematical language for measures, temporal signals, spatial fields, and, with suitable adaptations, complex networks. Its interpretation nevertheless depends on how the support, the measure, and the notion of scale are defined. This dependence becomes increasingly important as the analysis moves away from classical geometric measures toward symbolic and computational systems.

### *3.1. From Local Scaling to Multifractal Spectra*

Consider a normalized measure distributed over a support covered by elements of linear scale $\epsilon$. If $\mu_i(\epsilon)$ denotes the mass associated with the $i^{\text{th}}$ element, local scaling is expressed as

$$\mu_i(\epsilon) \sim \epsilon^{\alpha_i}, \tag{1}$$

where $\alpha_i$ is the local singularity or Hölder exponent. Halsey et al. formalized the corresponding distribution of singularities by introducing the spectrum $f(\alpha)$, which characterizes the fractal dimension of the subset associated with a given local exponent [3].

More precisely, the pointwise scaling exponent at a location $x$ of the support can be defined, whenever the limit exists, as $\alpha(x) = \lim_{\epsilon \to 0} \log \mu(B(x,\epsilon)) / \log \epsilon$, where $B(x,\epsilon)$ denotes a neighborhood of radius $\epsilon$. The points exhibiting a given local exponent form a level set $E_\alpha$, whose Hausdorff dimension defines the geometric singularity spectrum

$$E_\alpha = \{x \in \operatorname{supp} \mu : \alpha(x) = \alpha\}, \qquad f_{\text{geom}}(\alpha) = \dim_{\text{H}}(E_\alpha). \tag{2}$$

The abscissa $\alpha$ therefore identifies a local scaling strength, whereas the ordinate $f_{\text{geom}}(\alpha)$ measures the fractal extent of the subset exhibiting that strength. Larger values of $f_{\text{geom}}(\alpha)$ correspond to scaling classes occupying higher-dimensional subsets of the support; smaller values indicate geometrically less extensive classes.

A moment-based route to the spectrum starts from the partition function

$$Z(q,\epsilon) = \sum_i \mu_i(\epsilon)^q \sim \epsilon^{\tau(q)}, \tag{3}$$

where $q \in \mathbb{R}$ is the moment order and $\tau(q)$ is the mass-scaling exponent. Positive values of $q$ increase the contribution of regions carrying larger mass, while negative values emphasize weakly populated regions and are especially sensitive to finite sampling and numerical instability.

For $q \neq 1$, the generalized dimensions are defined by

$$D_q = \frac{\tau(q)}{q-1}, \tag{4}$$

while the information dimension $D_1$ is defined directly from the Shannon entropy of the measure as [2,3]

$$D_1 = \lim_{\epsilon \to 0} \frac{\sum_i \mu_i(\epsilon) \ln \mu_i(\epsilon)}{\ln \epsilon}. \tag{5}$$

Since $\tau(1) = 0$ for a normalized measure, Equation (5) coincides with the limit of Equation (4) as $q \to 1$ [2]. The familiar box-counting ($D_0$), information ($D_1$), and correlation ($D_2$) dimensions appear as special cases of the generalized family, while a monofractal measure is characterized by a $q$-independent $D_q$ and a linear $\tau(q)$. A multifractal measure is characterized by a nonlinear mass exponent and a nontrivial distribution of local singularities over the range in which the formalism is valid.

When $\tau(q)$ is differentiable and the Legendre construction is appropriate, the singularity strength associated with each moment order is

$$\alpha(q) = \frac{d\tau(q)}{dq}, \tag{6}$$

and the singularity spectrum follows as

$$f(\alpha) = q\alpha - \tau(q). \tag{7}$$

The Legendre-derived spectrum agrees with the geometrically defined $f_{\mathrm{geom}}(\alpha)$ when the multifractal formalism holds. Under standard regularity assumptions, it otherwise provides a concave upper bound and need not resolve nonconcave features of the geometric spectrum [22].

The Legendre formulation is compact and widely used, although it reconstructs the spectrum indirectly from the scaling function. Chhabra and Jensen introduced a direct method based on $q$-dependent normalized measures, allowing $\alpha$ and $f(\alpha)$ to be estimated without first computing the generalized dimensions and subsequently applying a numerical Legendre transform [26]. The two routes express the same underlying objective—resolving the distribution of scaling exponents—while differing in numerical implementation and in their sensitivity to finite data.

Figure 2 summarizes the geometric reading of the singularity spectrum used throughout this review. Under the differentiable Legendre construction, the local slope satisfies $df/d\alpha = q$. The point $q = 0$ therefore identifies the maximum $f(\alpha_0) = D_0$, whereas at $q = 1$, one obtains $f(\alpha_1) = \alpha_1 = D_1$, so that the identity line $f(\alpha) = \alpha$ is tangent to the spectrum at $\alpha_1$. The endpoints shown in the schematic correspond to a finite analyzed range $q \in [q_{\min}, q_{\max}]$ and consequently need not have zero ordinate. We denote by $\alpha_-$ and $\alpha_+$ the lower and upper singularity strengths attained over that range, so that the total width $\Delta\alpha = \alpha_+ - \alpha_-$ summarizes their spread. To quantify unequal left and right branches, we adopt the normalized asymmetry

$$\Delta\alpha_{\mathrm{L}} = \alpha_0 - \alpha_-, \qquad \Delta\alpha_{\mathrm{R}} = \alpha_+ - \alpha_0, \qquad A_\alpha = \frac{\Delta\alpha_{\mathrm{L}} - \Delta\alpha_{\mathrm{R}}}{\Delta\alpha_{\mathrm{L}} + \Delta\alpha_{\mathrm{R}}}, \tag{8}$$

for which $A_\alpha = 0$ indicates equal branch widths, $A_\alpha > 0$ a wider left branch, and $A_\alpha < 0$ a wider right branch. This convention is used only as a compact geometric descriptor and does not assign a universal physical interpretation to either branch.

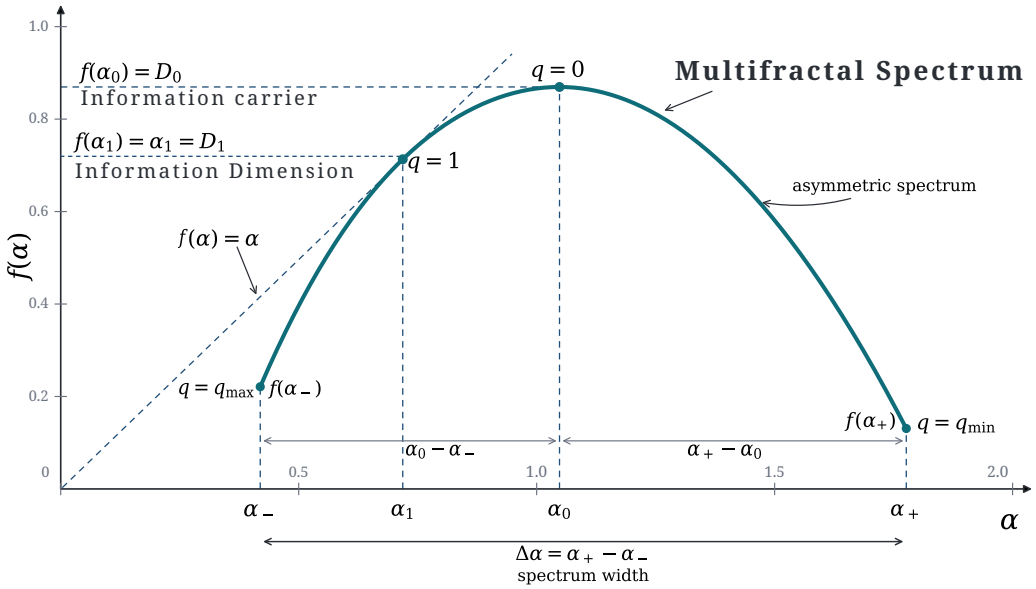


**Figure 2.** Schematic multifractal singularity spectrum $f(\alpha)$. The maximum at $q = 0$ identifies $f(\alpha_0) = D_0$, while the point associated with $q = 1$ satisfies $f(\alpha_1) = \alpha_1 = D_1$ and is tangent to the line $f(\alpha) = \alpha$. The width $\Delta\alpha = \alpha_+ - \alpha_-$ summarizes the spread of singularity strengths, and the unequal left and right branches illustrate spectral asymmetry. The endpoints correspond to a finite range of moment orders, $q \in [q_{\min}, q_{\max}]$, so $f(\alpha_-)$ and $f(\alpha_+)$ need not vanish.

### *3.2. Time-Series and Wavelet-Based Formulations*

Temporal data require an operational definition of scale that accommodates nonstationarity and trends. MF-DFA addresses this problem by integrating the demeaned signal, dividing the resulting profile into segments of length $s$, removing a local polynomial trend from each segment, and evaluating a $q$-order fluctuation function. If $F_q(s)$ denotes the resulting fluctuation function, scale dependence is written as

$$F_q(s) \sim s^{h(q)}, \tag{9}$$

where $h(q)$ is the generalized Hurst exponent [5]. A monofractal process exhibits an approximately constant $h(q)$ over the relevant moment range, whereas systematic $q$ dependence indicates that fluctuations of different magnitudes scale differently. This formulation has become particularly influential because detrending allows scaling analysis to be applied to many empirical records that cannot be treated as stationary over the full observation interval.

The connection between MF-DFA and the partition-function formalism requires explicit assumptions. For stationary signals with compact support under the standard construction used by Kantelhardt et al., the two sets of exponents satisfy

$$\tau(q) = qh(q) - 1. \tag{10}$$

Combining Equation (10) with the Legendre relations yields

$$\alpha(q) = h(q) + q\frac{dh(q)}{dq}, \qquad f(\alpha) = q[\alpha - h(q)] + 1. \tag{11}$$

These expressions are useful for translating between time-series and measure-based descriptions, while their domain of validity should be retained whenever the analysis departs from the assumptions under which the relation was derived. Practical MF-DFA

also introduces methodological choices concerning detrending order, segment sizes, and moment range, whose inferential consequences are examined in Section 4.

A complementary representation of local singularity is provided by wavelet methods, among which the wavelet transform modulus maxima (WTMM) formalism tracks maxima of wavelet coefficients across scales and constructs partition functions from the resulting maxima lines, thereby linking local regularity to a global multifractal spectrum [27,28]. WTMM is well suited to singular or irregular signals because the wavelet transform localizes structures in both position and scale. MF-DFA, WTMM, direct singularity-spectrum estimation, and classical partition functions share the objective of characterizing heterogeneous scaling while operating on distinct representations of the data. Comparative analyses have shown that these approaches are conceptually related without being rigorously interchangeable in all settings [22,29,30]. Extensions based on moving-average detrending and multifractal cross-correlation analysis further enlarge the estimator family and its range of admissible observables [31].

A complementary formulation, developed for multiplicative cascade processes in turbulence and geophysics, characterizes a conserved flux $\varepsilon_\lambda$ observed at scale ratio $\lambda = L/l > 1$, where $L$ is the largest scale of interest and $l$ the resolution, through the moment scaling function $K(q)$ [32,33]:

$$\langle \varepsilon_\lambda^q \rangle \sim \lambda^{K(q)}, \tag{12}$$

with $K(1) = 0$ for a normalized cascade. Singularities are written as $\varepsilon_\lambda \approx \lambda^\gamma$, and their codimension function $c(\gamma)$, defined by $\Pr(\varepsilon_\lambda \geq \lambda^\gamma) \approx \lambda^{-c(\gamma)}$, is related to $K(q)$ by the Legendre transform $c(\gamma) = \max_q[q\gamma - K(q)]$ [32,33]. For a cascade in an $E$-dimensional embedding space, the measure of a box of size $\epsilon = \lambda^{-1}$ is $\mu_i = \varepsilon_\lambda \lambda^{-E}$, and Equation (3) gives $Z(q, \epsilon) \sim \lambda^E \lambda^{-qE} \langle \varepsilon_\lambda^q \rangle = \lambda^{K(q)-(q-1)E}$. With the sign convention for $\tau(q)$ adopted here, this yields

$$K(q) = (q-1)E - \tau(q), \tag{13}$$

which reduces to $K(q) = q - 1 - \tau(q)$ for $E = 1$. The corresponding singularity strength and spectrum are $\alpha = E - \gamma$ and $f(\alpha) = E - c(\gamma)$ and [33] writes the same relation as $\tau_D(q) = K(q) - (q-1)D$, that is, with the opposite sign convention for $\tau$. Because $K$, $\gamma$, and $c$ do not depend on the dimension of the observing space, this codimension formulation is suited to stochastic processes and avoids the negative dimensions that arise in the $f(\alpha)$ description when $c(\gamma) > E$ [33]. For stable and attractive (universal) multifractal cascades, the moment scaling function reduces to two parameters [32,33]:

$$K(q) = \begin{cases} \dfrac{C_1}{\alpha_{\text{Lévy}} - 1}(q^{\alpha_{\text{Lévy}}} - q), & \alpha_{\text{Lévy}} \neq 1, \\ C_1\, q \ln q, & \alpha_{\text{Lévy}} = 1, \end{cases} \tag{14}$$

valid for $q > 0$ when $\alpha_{\text{Lévy}} \neq 2$, where $C_1 = \lim_{q\to 1} K(q)/(q-1) = K'(1)$, assuming differentiability at $q = 1$, is the continuous extension at $q = 1$ of the moment codimension function $C(q) = K(q)/(q-1)$ [32] and $0 \leq \alpha_{\text{Lévy}} \leq 2$ is the Lévy index, which interpolates between the $\beta$-model ($\alpha_{\text{Lévy}} = 0$) and the lognormal model ($\alpha_{\text{Lévy}} = 2$) [33]. The subscript distinguishes the Lévy index from the singularity strength $\alpha$, a distinction also stressed in [33]. These parameters can be estimated through trace-moment and double-trace-moment analyses [32,33]; applied to turbulent velocity data, the latter gives $\alpha_{\text{Lévy}} \approx 1.3 \pm 0.1$ and $C_1 \approx 0.25 \pm 0.05$ [33].

### *3.3. Support, Measure, Scale, and Estimator*

The common structure underlying these methods can be expressed through four ingredients that determine what a multifractal statement refers to. Let

$$\mathfrak{M} = (\mathcal{S}, \mu, \rho, \mathcal{E}), \tag{15}$$

where $\mathcal{S}$ denotes the support on which the analysis is defined, $\mu$ the measure or observable distributed over that support, $\rho$ the scale construction or resolution rule appropriate to the support, and $\mathcal{E}$ the estimator or formalism applied to recover the scaling quantities. Equation (15) is used here as an organizational notation rather than as a new definition of multifractality. Its purpose is to make explicit the modeling choices that remain implicit in many applications.

For a classical measure on a geometric set, $\mathcal{S}$ and $\rho$ may be specified by Euclidean boxes and their linear size. For a time series, the support is ordered temporally and scale is represented by segment length or wavelet dilation. For a network, graph distance, box-covering diameter, or a geometric embedding can supply competing notions of scale, each inducing a different relationship between the measured mass and the underlying topology. These distinctions become still more consequential for learning systems, where the candidate support may consist of parameters, neurons, interactions, hidden representations, or an optimization landscape. The same notation provides a bridge between the classical formalism summarized in Table 1 and the changes of locus examined in Sections 6 and 9.

Table 1 consequently groups the approaches by analytical object and identifies the support separately from the estimator and its scale construction. MF-DFA and WTMM appear together because both can analyze one-dimensional signals, although detrended fluctuations and wavelet-modulus maxima define different operational routes to scaling estimates; a common input support alone does not establish equivalence of the induced measures or spectra. In this classification, partitions and neighborhood metrics belong to the scale construction $\rho$, rather than to the support $\mathcal{S}$.

**Table 1.** Multifractal approaches grouped by analytical object. The support is distinguished from the estimator and its associated scale construction, allowing comparison of methods acting on a common support.

| Analytical Object | Support $\mathcal{S}$ | Estimator $\mathcal{E}$ and Scale $\rho$ | Main Quantities | Interpretive Constraints |
|---|---|---|---|---|
| **Measures and cascade fields** | | | | |
| Multifractal measure | Geometric set carrying the measure | Partition-function formalism [3]; box size $\epsilon$ | $Z(q,\epsilon)$, $\tau(q)$, $D_q$, $f(\alpha)$ | Requires a specified mass and cover; estimates depend on the accessible scaling range. |
| Multifractal measure | Geometric set carrying the measure | Direct singularity-spectrum estimation [26]; box size $\epsilon$ | $\alpha(q)$, $f(\alpha)$ | Uses normalized $q$-dependent masses; sampling and moment range constrain inference. |
| Multiplicative-cascade flux | Spatial or temporal domain | Universal multifractals; trace/double-trace moments [32,33]; resolution $\ell$ | $K(q)$, $c(\gamma)$, $C_1$, $\alpha_{\text{Lévy}}$ | Two-parameter description under the universality hypothesis; high-order moments face sampling limits or divergence. |

**Table 1.** *Cont.*

| Analytical Object | Support $\mathcal{S}$ | Estimator $\mathcal{E}$ and Scale $\rho$ | Main Quantities | Interpretive Constraints |
|---|---|---|---|---|
| **One-dimensional signals and functions** | | | | |
| One-dimensional signal | Ordered one-dimensional domain | MF-DFA [5,34]; segment length $s$ | $F_q(s)$, $h(q)$, $\tau(q)$, $f(\alpha)$ | Detrending, crossovers, record length, moments, and distributional effects influence inference. |
| One-dimensional signal | Ordered one-dimensional domain | WTMM [27,28]; wavelet dilation $a$ | Maxima-line partition functions, $\tau(q)$, $f(\alpha)$ | Wavelet and maxima-line choices, together with limited scaling ranges, affect the estimate. |
| **Networks** | | | | |
| Unweighted or weighted network | Graph vertex set | Graph-distance sandbox [35,36]; radius $r$ | $D_q$, $\tau(q)$ | Depends on graph metric, center selection, and available network diameter. |
| Spatially embedded network | Graph vertex set | Geometric sandbox [37]; geometric radius $r$ | $D_q$, $f(\alpha)$ | Coordinates enter the scale rule; estimates reflect embedding as well as connectivity. |
| Hyperbolically embedded network | Graph vertex set | Embedding-derived edge weights and weighted sandbox [38]; weighted radius $r$ | $D_q$ | The weighted distance couples topology and latent geometry; the weight construction affects $D_q$. |

The compact notation summary in Table 2 consolidates the symbols introduced in this section and used in the subsequent discussion. It is deliberately focused on the multifractal formalism and on the support–measure–scale construction, so that framework-specific notation is introduced only where it becomes conceptually necessary.

**Table 2.** Notation used in the multifractal formalism.

| Symbol | Meaning |
|---|---|
| $q$ | Moment order in a multifractal partition or fluctuation function. |
| $\epsilon$ or $s$ | Spatial or temporal scale, according to the analysis setting. |
| $\mu_i(\epsilon)$ | Measure associated with the $i^{\text{th}}$ element of a partition at scale $\epsilon$. |
| $Z(q,\epsilon)$ | Multifractal partition function. |
| $\tau(q)$ | Mass-scaling exponent. |
| $D_q$ | Generalized dimension of order $q$. |
| $h(q)$ | Generalized Hurst exponent in MF-DFA. |
| $K(q)$ | Moment scaling function of a cascade, Equation (12). |
| $\gamma$, $c(\gamma)$ | Order of singularity and its codimension function in the cascade formulation. |
| $C_1$, $\alpha_{\text{Lévy}}$ | Universal multifractal parameters, Equation (14). |
| $\alpha$ | Local singularity or Hölder exponent. |
| $\alpha_0$ | Singularity strength at the maximum of $f(\alpha)$. |
| $\alpha_-$, $\alpha_+$ | Lower and upper singularity strengths attained over the analyzed moment range. |
| $f(\alpha)$ | Singularity spectrum. |
| $\Delta\alpha$ | Width of the singularity spectrum, $\alpha_+ - \alpha_-$. |
| $A_\alpha$ | Normalized spectral asymmetry defined in Equation (8). |
| $\mathfrak{M}$ | Analysis object used in Equation (15). |
| $\mathcal{S}$ | Support on which the multifractal analysis is defined. |
| $\mu$ | Measure or observable distributed over the support $\mathcal{S}$. |
| $\rho$ | Scale construction or resolution rule used for the chosen support. |
| $\mathcal{E}$ | Estimator or multifractal formalism applied to the analysis object. |

Supplementary Table S1 provides a domain-oriented counterpart to this object-based classification, summarizing representative estimators, methodological alternatives, and conditions for meaningful comparisons across application areas. The table documents methodological choices rather than ranking estimator accuracy across heterogeneous data and supports.

Estimator dependence can be examined under controlled conditions by holding the signal class and record length fixed while varying the analysis formalism. Figure 3 compares MF-DFA with a canonical WTMM construction using first- and second-order derivative-of-Gaussian (DOG) wavelets, denoted DOG1 and DOG2. In the WTMM calculations, the integrated signal profile is analyzed, modulus maxima are linked across scales into maxima lines, and the running supremum along each line enters the partition function, following the classical formulation and the comparative protocol used in the literature [27,28,30]. Both controlled references have length $N = 2^{16}$. Fractional Gaussian noise with $H = 0.70$ provides the monofractal case, while a binomial $p$-model with $p = 0.30$ provides a multifractal measure with a known theoretical spectrum [39]. Each small point is the median over 10 independent realizations for one of nine validated analysis settings obtained from three scale configurations and three moment ranges. The large marker and vertical bar summarize the median and interquartile range across those nine setting-level estimates, respectively.

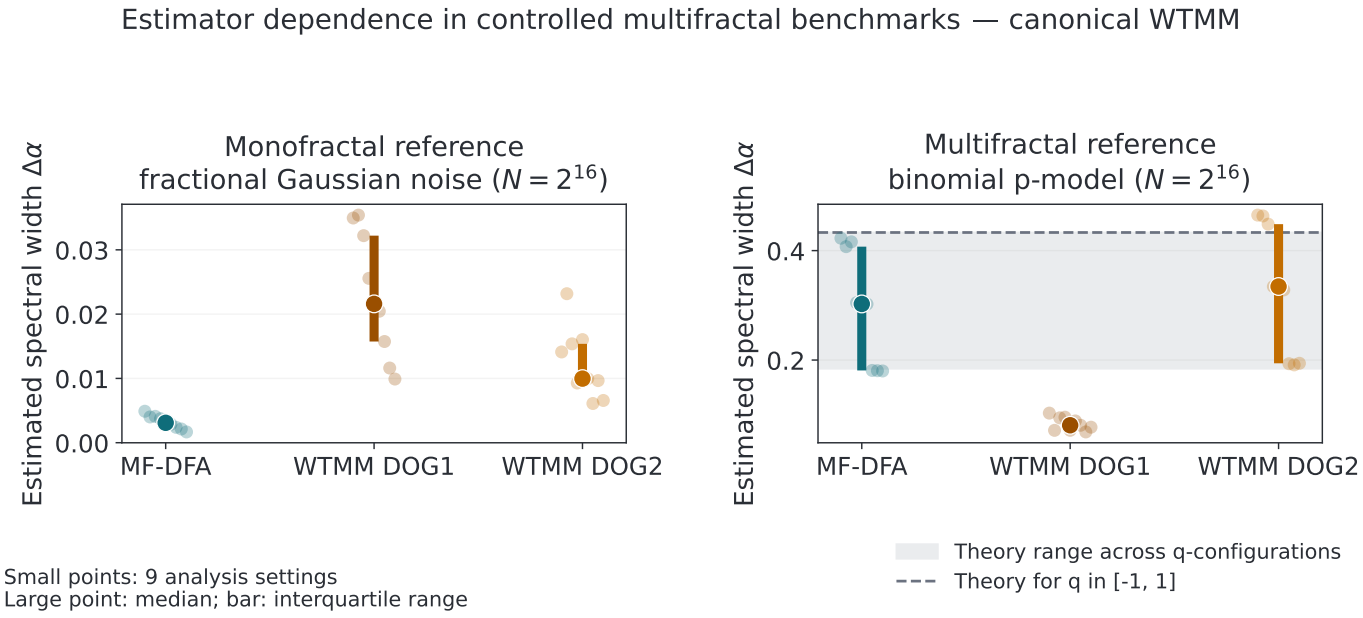


**Figure 3.** Controlled benchmark illustrating estimator dependence using a canonical WTMM construction. MF-DFA is compared with WTMM using DOG1 and DOG2 wavelets on fractional Gaussian noise with $H = 0.70$ and a binomial $p$-model with $p = 0.30$, both at $N = 2^{16}$. WTMM is applied to the integrated profile; modulus maxima are linked across scales into maxima lines and the running supremum along each line is used in the partition function. Each small point denotes the median estimated spectral width $\Delta\alpha$ over 10 independent realizations for one of nine validated settings combining three scale configurations and three moment ranges; the large marker and vertical bar denote the median and interquartile range across the nine setting-level estimates. In the $p$-model panel, the gray band spans the theoretical widths induced by the three validated moment ranges, while the dashed line marks the theoretical width for $q \in [-1, 1]$. The benchmark illustrates dependence on estimator and wavelet choice and is not intended as a general performance ranking.

On the fractional-Gaussian-noise reference, MF-DFA remains close to zero spectral width across the validated settings, whereas both canonical WTMM variants retain a modest finite-sample broadening. The $p$-model reveals a different pattern. MF-DFA and WTMM with DOG2 remain comparatively close to the configuration-specific theoretical widths, whereas WTMM with DOG1 substantially underestimates them over the validated settings. Estimator dependence therefore cannot be reduced to a monotonic tendency of WTMM to broaden spectra. The inferred $\Delta\alpha$ depends on the analysis formalism, the analyzing wavelet, and the moment and scale ranges used in the fit. The gray band in the right panel spans the theoretical values of $\Delta\alpha$ induced by the three validated moment ranges, while the dashed line marks the theoretical width for $q \in [-1, 1]$. Neither element represents an uncertainty interval. These results make the role of the estimator $\mathcal{E}$ in Equation (15) explicit and are intended as a controlled methodological illustration rather than as a general ranking of MF-DFA and WTMM [5,22,30].

## 4. From Apparent to Supported Multifractality

A multifractal spectrum supports a stronger scientific interpretation only when the observed scale dependence is assessed against effects introduced by finite sampling, distributional heterogeneity, preprocessing choices, and estimator-specific assumptions. This distinction is especially important for empirical time series, where a broad singularity spectrum may arise from several interacting sources and where the accessible scaling range is necessarily finite. We denote the width of the spectrum by

$$\Delta\alpha = \alpha_+ - \alpha_-, \tag{16}$$

where $\alpha_-$ and $\alpha_+$ stem from Section 3. Together with the asymmetry $A_\alpha$ defined in Equation (8), the width is best treated as a summary descriptor whose interpretation depends on the construction of the signal, the estimator, the analyzed moment range, and the validation strategy. The formalisms summarized in Section 3 provide complementary routes to the same general problem, while their practical outputs remain sensitive to different aspects of the data and are not mathematically interchangeable in every setting [22]. A critical review of multifractal evidence consequently requires a distinction between the detection of heterogeneous scaling and the attribution of that scaling to a persistent property of the generating process.

Figure 4 summarizes the inferential structure developed in this section. An observed multifractal signature motivates further analysis because temporal correlations, distributional heterogeneity, finite-size effects, trends and crossovers, estimator dependence, and preprocessing choices can all contribute to the measured spectrum, leaving the explanation underdetermined until additional controls are introduced. Scaling stability, uncertainty analysis, surrogate testing, finite-size assessment, cross-method validation, and mechanistic support progressively constrain the set of defensible interpretations. The resulting claim should be calibrated to the available evidence, ranging from an empirical observation of multifractality to source-constrained or mechanistically supported interpretations when the corresponding controls are available.

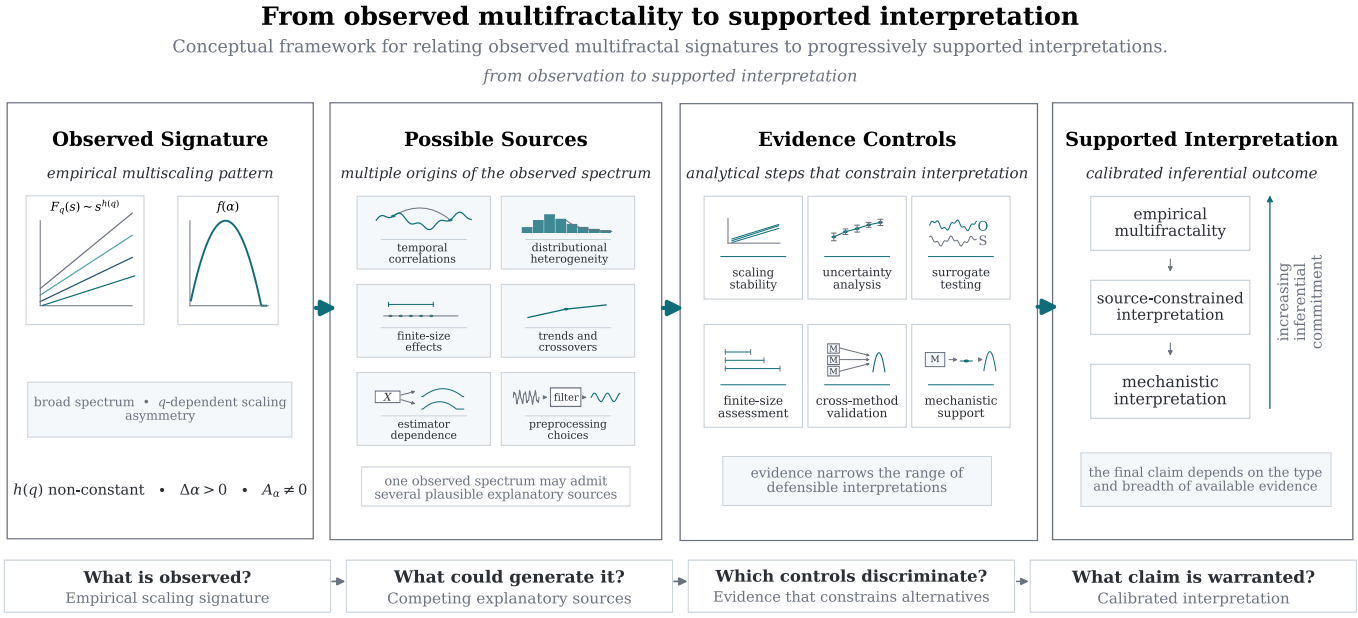


**Figure 4.** Conceptual framework for moving from an observed multifractal signature to a supported interpretation. A broad spectrum or $q$-dependent scaling pattern can reflect multiple sources, including temporal correlations, distributional heterogeneity, finite-size effects, trends and crossovers, estimator dependence, and preprocessing choices. Evidence from scaling stability, uncertainty analysis, surrogate testing, finite-size assessment, cross-method validation, and mechanistic support progressively constrains the interpretations that can be defended. The resulting claim may remain at the level of empirical multifractality or, when the corresponding evidence is available, support source-constrained or mechanistic interpretation. The sequence represents increasing inferential commitment rather than a universal quality ranking.

### *4.1. Sources of Apparent Multifractality*

Finite data length is one of the most general sources of uncertainty because multifractal estimation relies on moments evaluated over a restricted range of scales. The tails of the singularity spectrum are particularly sensitive to rare fluctuations, and the effect becomes stronger when large positive or negative moment orders are included. Positive moments emphasize regions associated with large fluctuations, whereas negative moments amplify the contribution of weak fluctuations and sparsely populated regions of the measure. In finite samples, these regions may be poorly represented and can produce unstable estimates of $h(q)$, $\tau(q)$, or $f(\alpha)$. The choice of the moment interval and of the scaling window consequently forms part of the inferential problem, with finite-size normalization and the selected range of moment orders capable of materially changing the inferred spectral spread [40,41].

Comparable caution is required for trends, crossovers, and nonstationarities. Although MF-DFA is designed to reduce the influence of polynomial trends, the estimated scaling exponents still depend on detrending order and on the available range of window sizes [5,34]. Characteristic scales can also interrupt an otherwise approximate power law. Crossovers can reflect genuine transitions between dynamical regimes, although they can also arise from periodic components, preprocessing, or insufficient separation between the lower and upper bounds of the scaling range [42,43]. De Santis et al. [44] demonstrated that Fourier-domain smoothing can mitigate periodicity-induced crossovers in MF-DFA, using synthetic and sunspot records, and subsequently applied the procedure to medium-voltage feeder-current data. A spectrum reconstructed across a poorly resolved crossover may combine distinct scaling regimes into a single apparent multifractal signature.

A second source of ambiguity arises from distributional heterogeneity, since heavy-tailed fluctuations can substantially broaden the empirical spectrum, particularly in finite records, and early discussions of multifractal time series often treated the distribution of fluctuations and temporal correlations as two largely independent generators of multifractality. Empirical decompositions have shown that the relative contribution of distributional and temporal effects is strongly process dependent [45], while more recent work has sharpened the asymptotic interpretation. Within the MF-DFA setting analyzed by Kwapień et al. [19], uncorrelated series from the Gaussian basin of attraction lose the apparent multifractal broadening asymptotically as the sample length increases, while Lévy-stable fluctuations lead to bifractal rather than genuinely multifractal behavior. The authors consequently identify long-range temporal correlations as the essential source of genuine multifractality in the class of processes considered, with heavy tails modulating the width of the spectrum when those correlations are present. Kluszczyński et al. [20] later developed controlled cascade experiments in which the fluctuation distribution is varied while the correlation structure is retained, further quantifying the influence of tail thickness on the observed spectral width. These results provide a stronger basis for source attribution, while their conclusions remain tied to the specific stochastic constructions and multifractal estimators under study.

Finite-size artifacts can become even more pronounced in discrete systems. Jaroszewicz et al. [21] examined the two-dimensional Ising model and showed that broad singularity spectra previously interpreted as multifractal can be dominated by lattice discreteness and finite-size effects, especially in the negative-$q$ regime. After restricting the analysis to positive moments and performing systematic finite-size scaling, the estimated spectral width decreases toward zero in the thermodynamic limit for the analyzed settings. The result illustrates a general inferential principle without implying that all finite systems are spuriously multifractal. A nonzero estimated $\Delta\alpha$ at one system size records an empirical spectral spread, while persistence under increasing size or record length is required before that spread can support a stronger structural interpretation.

### *4.2. Disentangling Sources and Testing Robustness*

Source attribution becomes more reliable when the original data are compared with surrogate series constructed to preserve selected statistical properties while disrupting others. The surrogate-data framework was introduced to test explicit null hypotheses about the dynamics of observed time series [46]. Later developments emphasized that the interpretation of a surrogate test depends on the null model being represented faithfully and on the discrimination statistic being sensitive to the property of interest [47,48]. In multifractal studies, random shuffling is particularly useful because it destroys temporal ordering while preserving the empirical distribution of the observed values exactly. A marked contraction of the multifractal spectrum after shuffling supports an interpretation in which temporal dependence contributes materially to the original scaling structure.

Phase-randomized, amplitude-adjusted Fourier-transform (AAFT), and iterative amplitude-adjusted Fourier-transform (IAAFT) surrogates address related but distinct null-model requirements. Fourier phase randomization preserves the power spectrum, and hence the linear autocorrelation structure, while generally changing the empirical amplitude distribution. AAFT surrogates seek to accommodate the observed distribution, whereas IAAFT procedures improve simultaneous agreement with the amplitude distribution and target spectrum [47,48]. Agreement between the original record and an appropriately constructed surrogate weakens claims that the detected multifractality requires structure excluded by the corresponding null model, whereas systematic departure provides evidence against that null. These tests remain conditional rather than absolute,

and surrogate generation can itself introduce biases when the assumptions of the null model are poorly matched to the data [48]. The evidential value derives from the relation between the scientific hypothesis and the statistical property preserved by the surrogate.

Robustness also depends on explicit uncertainty analysis, with bootstrap or Monte Carlo resampling providing estimates of the variability of exponents and spectrum widths while repeated estimation over plausible moment ranges, detrending orders, and scaling intervals reveals sensitivity to analysis choices. When several independent realizations, subjects, spatial samples, or temporal segments are available, the persistence of the inferred spectrum across them provides an additional test of reproducibility. This form of replication is especially valuable for stochastic systems because a single realization can display a broad spectrum even when the ensemble behavior is substantially narrower. Cross-method comparisons provide another useful control when the same object admits more than one appropriate formulation. Agreement between MF-DFA, wavelet-based estimates, direct singularity-spectrum methods, or network-specific estimators can strengthen confidence that the observed structure is not an artifact of one implementation. Such agreement should be interpreted with care because the methods act on different mathematical representations and emphasize different aspects of the data [22]. Methodological convergence provides supporting evidence, whereas disagreement can be scientifically informative when it reveals dependence on support, measure, or scale construction.

To make the source-discrimination logic explicit under a common estimator, Figure 5 reports a controlled synthetic benchmark analyzed with MF-DFA. Four process classes were selected to separate finite-sample, distributional, and temporal effects. Gaussian white noise serves as the uncorrelated monofractal reference, whereas fractional Gaussian noise with $H = 0.80$ provides a long-memory monofractal case. An independent and identically distributed (i.i.d.) Student-$t$ process with $\nu = 3$ illustrates heavy-tail-induced finite-sample broadening in the absence of designed temporal dependence, while a correlated lognormal multifractal random walk (MRW)-type process supplies the controlled multifractal reference [5,19,49]. Across repeated realizations, the first two cases retain narrow spectra, while shuffling moves the fractional-Gaussian-noise spectrum toward the uncorrelated scaling location. The Student-$t$ broadening changes little under shuffling because the marginal distribution is preserved and the process contains no designed temporal organization. By contrast, the spectrum of the MRW-type process contracts substantially after shuffling, consistently with the removal of temporal organization contributing to its multifractal signature. These calculations are finite-sample illustrations of the inferential logic developed above and are not intended to define universal numerical thresholds for multifractality.

The scaling functions underlying the spectra in Figure 5 are shown in Figure 6. For each process, the original and shuffled realizations are displayed separately for representative orders $q = -2, 0, 2$ within the full analysis range $q \in [-3, 3]$. The curves summarize the same 32 realizations used for the singularity spectra, with pointwise interquartile bands and power-law fits over the analysis scales. The linearity observed in these finite-range log–log representations supports the estimation of $h(q)$ for the displayed orders; it does not by itself establish asymptotic scaling or stability at the extreme moment orders.

The complementary calculation in Figure 7 isolates the dependence of the estimated spectral width on record length while retaining the same MF-DFA analysis settings. Gaussian white noise, the i.i.d. Student-$t$ process with $\nu = 3$, and the correlated lognormal MRW-type process were evaluated at $N \in \{2^{10}, 2^{12}, 2^{14}, 2^{16}\}$ using 32 independent realizations at each length. The Gaussian reference contracts rapidly toward a narrow finite-sample floor as $N$ increases. The Student-$t$ process also narrows systematically, while remaining broader than the Gaussian reference over the analyzed range, consistently with heavy-tail-induced finite-sample broadening. The MRW-type process retains a comparatively

stable and broader spectrum at the largest sample length. These trajectories illustrate why persistence under increasing record length forms part of the evidential basis of a multifractal claim. Contraction can expose finite-size broadening, whereas persistence across the tested range provides stronger support for structured heterogeneous scaling without establishing its asymptotic form by itself. The magnitude and convergence of $\Delta\alpha$ remain process- and estimator-dependent, so the comparison should be read qualitatively rather than as a universal threshold [19,21,40].

To assess the scaling behavior underlying the finite-size comparison, Figure 8 presents the fluctuation functions at the shortest and longest record lengths. The diagnostic uses the same MF-DFA implementation and the same 32 realizations per process and length as Figure 7. The shorter records offer a markedly narrower interval of scales; consequently, the goodness of a log–log linear fit should be interpreted together with the available scale range rather than as evidence of size-independent exponents.

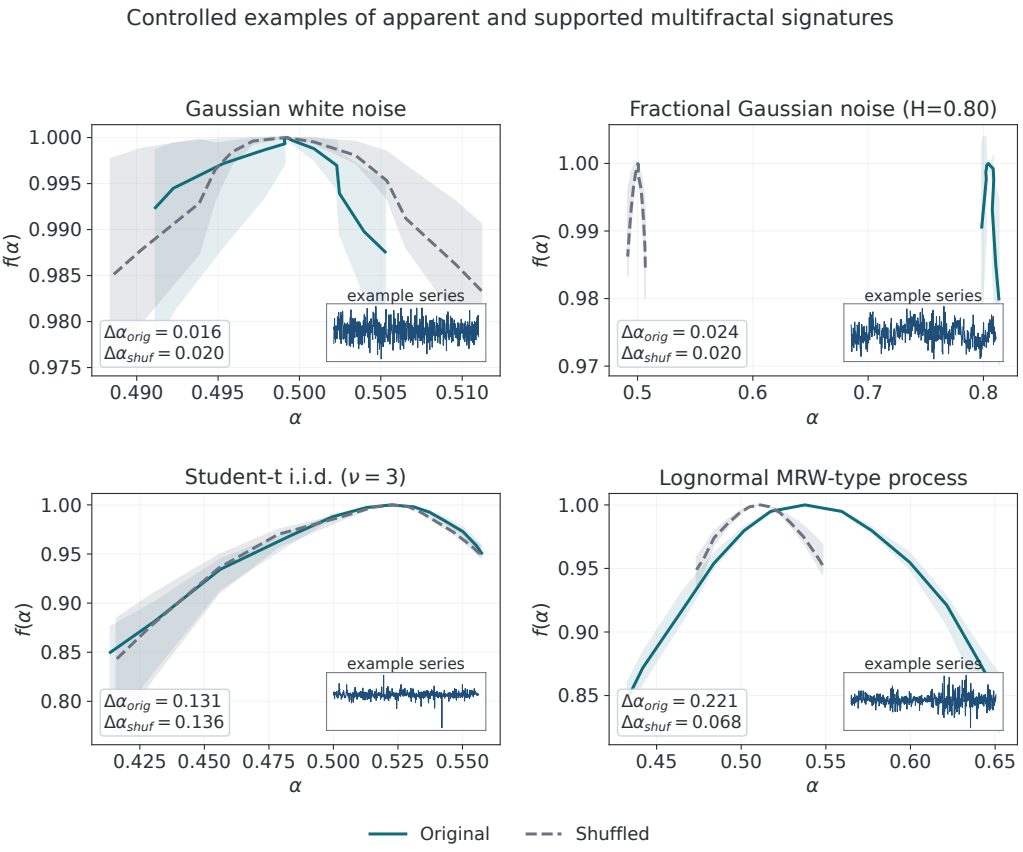


**Figure 5.** Controlled synthetic examples of apparent and supported multifractal signatures. Four process classes of length $N = 2^{15}$ were analyzed with MF-DFA using first-order detrending over $q \in [-3, 3]$ and 32 independent realizations per class. Solid curves show the pointwise median singularity spectrum estimated from the original realizations, dashed curves show the corresponding median after random shuffling, and shaded regions indicate interquartile variability. Random shuffling preserves the empirical amplitude distribution while destroying temporal ordering. Gaussian white noise provides an uncorrelated monofractal reference; fractional Gaussian noise with $H = 0.80$ isolates long-range dependence within a monofractal process; an i.i.d. Student-$t$ process with $\nu = 3$ illustrates heavy-tail-induced finite-sample broadening; and a correlated lognormal MRW-type process provides a controlled multifractal reference. The median values of $\Delta\alpha$ are reported within the panels. The examples illustrate source-discrimination logic and do not define numerical thresholds for multifractality.

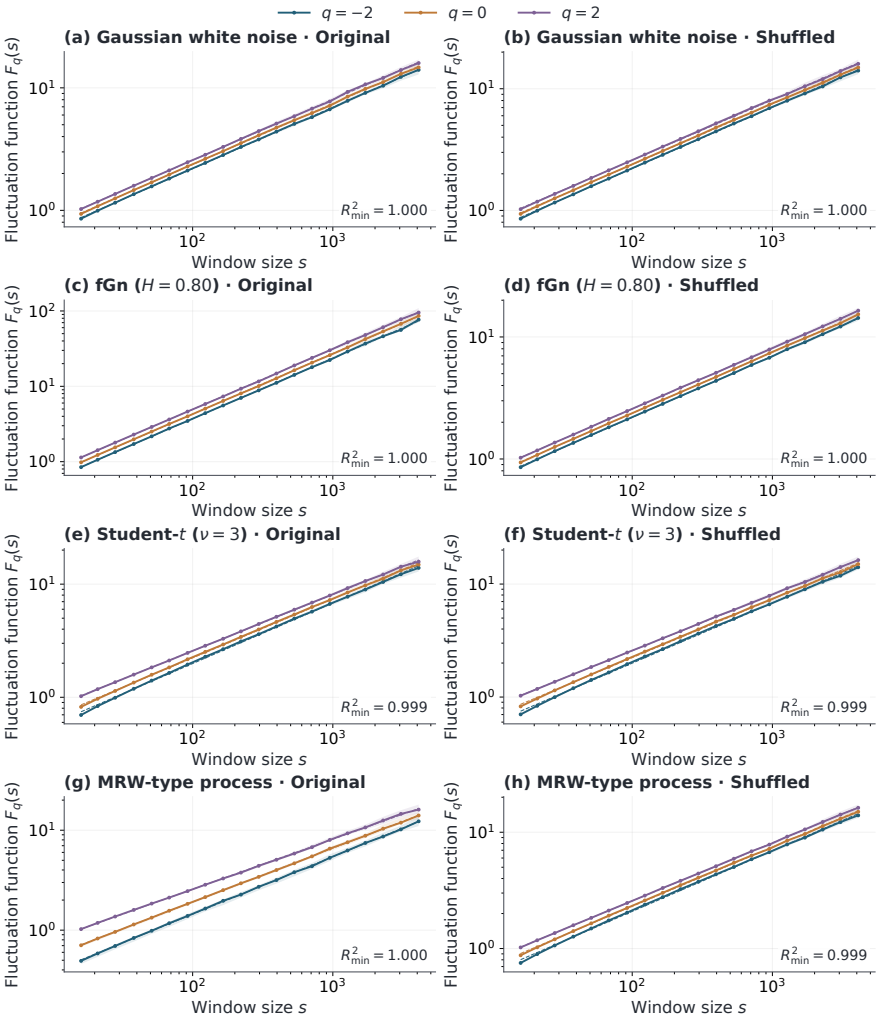


**Figure 6.** MF-DFA fluctuation functions underlying the source-discrimination benchmark (Figure 5). Rows show Gaussian white noise, fractional Gaussian noise ($H = 0.80$), i.i.d. Student-$t$ noise ($\nu = 3$), and the lognormal MRW-type process; columns show the original and shuffled series. Colored lines and markers represent pointwise medians of $F_q(s)$ over 32 independent realizations at $q = -2, 0, 2$, with translucent interquartile bands. Dashed lines are log–log linear fits to the median curves across the same 20 nominal window sizes (after integer rounding). Each panel reports the smallest coefficient of determination $R^2$ among its three displayed moment orders. Record length is $N = 2^{15}$, with first-order detrending. The displayed scaling ranges and fits are descriptive finite-sample diagnostics.

Because the main Student-$t$ control uses $\nu = 3$ over $q \in [-3, 3]$, we additionally tested whether the qualitative conclusions depend on the boundary $q = 3$ moment. Two robustness controls retained the same MF-DFA implementation and replication design. The first used Student-$t$ with $\nu = 3$ over $q \in [-2, 2]$, while the second used Student-$t$ with $\nu = 5$ over $q \in [-3, 3]$. In both cases, the Student-$t$ spectrum remained broader than the Gaussian reference, changed little under shuffling, and narrowed systematically with increasing $N$, while the MRW-type process retained the stronger shuffling-induced contraction and the broader spectrum at the largest tested record length. The qualitative interpretation of Figures 5 and 7 therefore does not depend on the boundary-moment configuration. The complete sensitivity results are reported in the Supplementary Material.

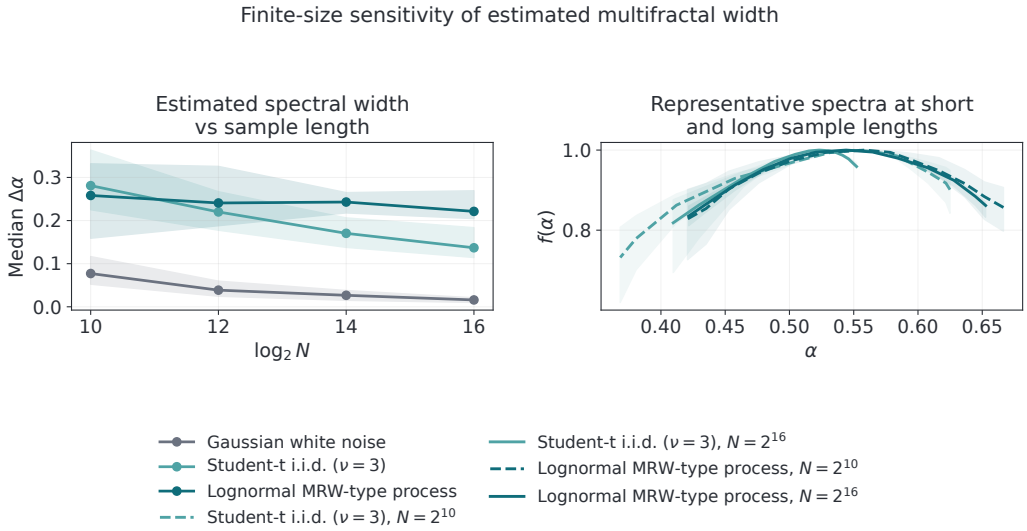


**Figure 7.** Finite-size sensitivity of estimated multifractal width. Left panel reports the median spectral width $\Delta\alpha$ as a function of sample length for Gaussian white noise, an i.i.d. Student-$t$ process with $\nu = 3$, and a correlated lognormal MRW-type process. Each point summarizes 32 independent realizations analyzed with MF-DFA using first-order detrending over $q \in [-3, 3]$; shaded regions indicate the interquartile range. Right panel compares the median singularity spectra $f(\alpha)$ of the Student-$t$ and MRW-type processes at the shortest and longest analyzed records, $N = 2^{10}$ and $N = 2^{16}$. The Gaussian reference contracts rapidly with increasing $N$, the Student-$t$ process exhibits progressive narrowing, and the MRW-type process retains a broader spectrum over the tested range. These controlled calculations illustrate finite-size sensitivity and do not define universal numerical thresholds or establish asymptotic multifractality.

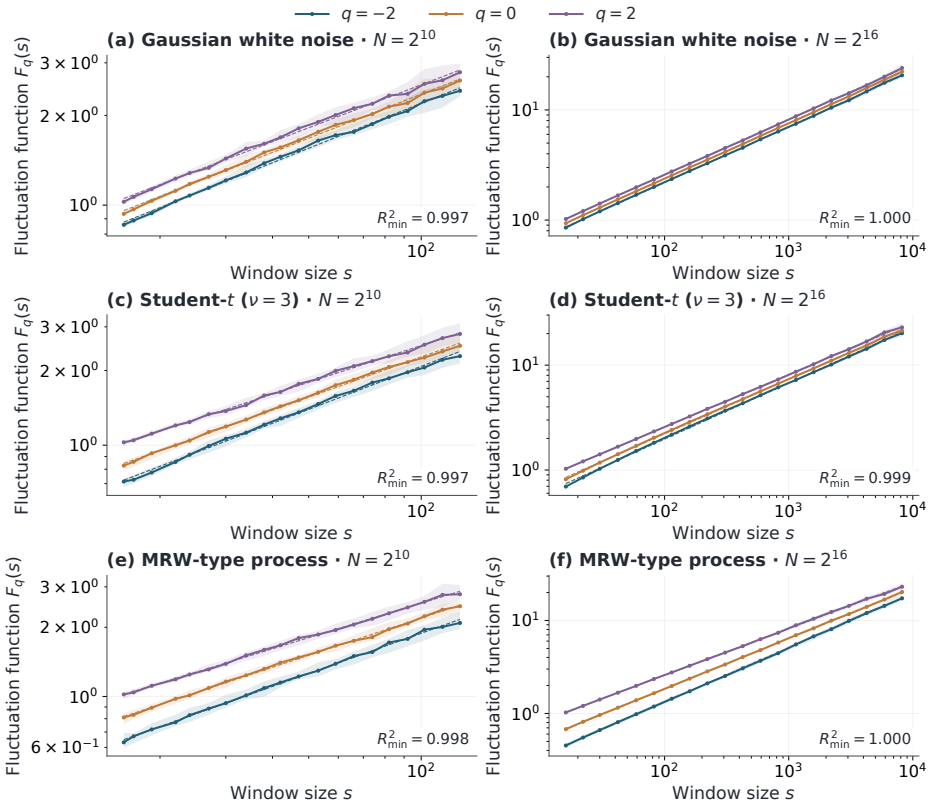


**Figure 8.** MF-DFA fluctuation functions for the finite-size benchmark (Figure 7). Gaussian white noise, i.i.d. Student-$t$ noise ($\nu = 3$), and the correlated lognormal MRW-type process are compared at $N = 2^{10}$ (left) and $N = 2^{16}$ (right). Solid colored curves with markers are the pointwise median $F_q(s)$ for $q = -2, 0, 2$ over 32 realizations, translucent bands show interquartile variability, and dashed lines indicate the corresponding log–log linear fits. The minimum $R^2$ among the three moment orders is reported in each panel. First-order detrending and the same nominal 20-scale construction as in the original analysis are used. The restricted scaling interval at $N = 2^{10}$ should be considered when interpreting the fitted exponents.

### *4.3. Evidence Dimensions for Multifractal Claims*

The literature considered above suggests that multifractal claims are better evaluated through several complementary dimensions of evidence than through a single threshold or quality score. The first concerns the existence and stability of scaling itself, which requires the relevant fluctuation functions, partition sums, or network measures to exhibit a defensible scaling region and a reproducible dependence on moment order. A second dimension concerns uncertainty, including the variability of estimated exponents, the sensitivity to parameter choices, and the stability of the spectrum across plausible analysis settings. Surrogate-based comparisons provide a third dimension by testing whether temporal ordering, linear dependence, nonlinear phase structure, or the marginal distribution account for the observed scaling. Finite-size or finite-length analysis addresses whether the inferred spectrum persists as more information becomes available. Cross-method validation evaluates the extent to which the conclusion survives changes in estimator or representation. Finally, mechanistic support connects the statistical signature to an independently motivated model of the underlying dynamics.

These dimensions describe different forms of support and need not appear together in every study. A mathematically derived multifractal measure can have strong mechanistic grounding without requiring surrogate testing, while an empirical time series can provide convincing surrogate and uncertainty analyses in the absence of a complete dynamical model. The distinction is particularly relevant for the applications discussed in Sections 5–9,

where the same language of multifractality is used for physical signals, symbolic sequences, networks, and learning systems. Throughout this review, the term *supported multifractality* therefore refers to a multifractal interpretation whose evidential basis is made explicit with respect to the object being studied and the scientific claim being advanced. This usage preserves the descriptive value of observed scaling while allowing stronger dynamical or mechanistic interpretations to be assessed according to the additional evidence they require.

## 5. Multifractality as a Probe of Structure, Memory, and Dynamics

Once the existence of heterogeneous scaling has been established with an evidential basis appropriate to the system under study, multifractal quantities can be used to investigate how variability is organized across scales. Their scientific role then extends beyond compact description. The dependence of scaling exponents on moment order can reveal whether large and small fluctuations are governed by comparable or distinct scaling laws, while the shape and width of the singularity spectrum provide a mesoscopic representation of how local regularities are distributed over the observed process. In many complex systems, this representation has been related to long-range dependence [8,50], intermittency [7,51,52], cascade organization [39,52,53], and changes in dynamical regime [6,8]. These interpretations acquire meaning through the combination of multifractal analysis with independent knowledge of the generating process and with the source-discrimination criteria discussed in Section 4.

### *5.1. Heterogeneous Scaling and Long-Range Organization*

The historical development of the multifractal formalism is closely connected to fully developed turbulence, where cascade models and intermittency analyses established a multiscale account of anomalous scaling before the formalism was generalized across domains [4,39,51,52,54]. In fully developed turbulence, intermittency causes velocity increments and energy dissipation to depart from a description based on a single scaling exponent. The multifractal approach models this heterogeneity through a continuum of local exponents associated with different regions of the flow, thereby providing a statistical representation of the nonuniform transfer of activity across scales [7]. In this setting, the spectrum has a direct physical motivation because intense and weak fluctuations contribute differently to the cascade, while the distribution of singularities summarizes the uneven organization produced by the underlying dynamics. Turbulence therefore illustrates a general principle that recurs throughout the field, whereby multifractality becomes scientifically informative when scale-dependent heterogeneity can be related to a process that redistributes fluctuations across scales.

A comparable logic appears in physiological dynamics, although the underlying mechanisms are different. Ivanov et al. [6] reported multifractal organization in healthy heartbeat intervals and showed that the nonlinear properties associated with this organization are encoded in Fourier-phase relations. The same study found a substantial loss of multifractality in congestive heart failure, suggesting that physiological regulation can involve a broad organization of fluctuations across timescales whose structure cannot be captured by a single characteristic exponent. This interpretation is consistent with the view of healthy physiology as the outcome of interacting control processes acting over multiple temporal scales, a perspective developed more broadly in work on fractal physiological dynamics and on the distinction between fractal noises and motions [55–57]. Later applications have extended multifractal analysis to other physiological signals, including blood-pressure dynamics, where persistent correlations and broad spectra have been used to characterize the temporal organization of cardiovascular regulation [58].

Financial time series provide a further example in which multifractality is connected to structured variability across scales. The literature reviewed by Jiang et al. [8] documents broad evidence of multifractal behavior in returns, volatility, and related market observables, together with an extensive discussion of heavy-tailed distributions, long-range dependence, and model-based explanations. The financial case is especially instructive because cascade analogies, multifractal random-process models, and surrogate decompositions have all been used to explain scale-dependent fluctuations [45,53,59]. It also exposes the interpretive ambiguity of a broad spectrum, since similar empirical signatures may reflect temporal correlations, heterogeneous distributions, market microstructure, or combinations of these factors. The multifractal quantities remain useful as descriptors of scale-dependent organization, while their dynamical meaning depends on the extent to which these sources are independently constrained.

Hydro-climatological records provide another established test bed for the same questions. River runoff and precipitation exhibit long-term persistence and non-universal multifractal behavior, while method comparisons and later reviews emphasize crossover scales, trends, and estimator choice [24,29,50].

Long-range organization extends beyond physical and financial signals to symbolic systems, where studies based on letters, sentences, word lengths, and multifractal spectra have repeatedly identified dependencies extending beyond local linguistic structure [60–65]. Multifractal analysis offers an additional description of this hierarchical dependence by resolving how fluctuations associated with symbolic organization vary across scales. In a comparative study of modern and ancient languages, De Santis et al. [66] mapped lexical categories into numerical sequences and reported persistent multifractal signatures associated with morphological organization, with the resulting descriptors carrying information about linguistic families. Recent surrogate constructions that preserve both Zipf-like frequency structure and long-range dependence further illustrate how null models can separate lexical statistics from higher-order symbolic organization [67]. The example is useful because the support is neither a directly measured physical trajectory nor a geometric object, and the observed scaling therefore depends on a representation that preserves selected aspects of symbolic structure. The interpretation therefore involves both the organization of the original text and the mapping through which that organization is made measurable.

### *5.2. From Statistical Signature to Dynamical Interpretation*

The examples above illustrate why multifractality and memory are often discussed together, while the two concepts retain distinct meanings. Long-range dependence concerns correlations that decay slowly enough for distant observations to remain statistically coupled over extended lags. Multifractality concerns the dependence of scaling behavior on fluctuation magnitude or local singularity strength. A process may exhibit long-range dependence with a single dominant scaling exponent, and a finite record may display an apparently broad spectrum without supporting a persistent multifractal structure. The scientific question concerns how temporal dependence, distributional heterogeneity, and cross-scale organization combine to produce the measured spectrum.

Multiplicative cascade models provide one of the clearest mechanisms linking dynamics and multifractal scaling. In turbulence, the transfer of energy across progressively smaller scales motivates cascade descriptions in which local intensities result from repeated multiplicative redistribution [7]. Related stochastic constructions, including MRWs, reproduce intermittent fluctuations and scale-dependent moments through an explicit coupling between volatility organization and temporal scale [49]. Such models are valuable because they connect a family of observed scaling exponents to a generative mechanism. Their

explanatory role depends on whether the assumptions of the cascade construction are plausible for the empirical system being analyzed.

Temporal correlations provide a second route from statistical description to dynamical interpretation. The surrogate logic developed in Section 4 allows this route to be tested by asking whether the spectrum contracts when temporal organization is disrupted while the relevant marginal properties are retained. This form of evidence is particularly useful for physiological, financial, and symbolic signals, where multifractal analysis can act as a diagnostic probe of structured heterogeneity whose source is then compared with domain-specific hypotheses.

Changes in the multifractal spectrum can also be interpreted as changes in regime when they occur together with independent evidence of altered system organization. A narrowing spectrum may indicate reduced heterogeneity of scaling, while shifts in its position or asymmetry can reflect changes in the relative contribution of weak and strong fluctuations, with the interpretation remaining system dependent. In physiology, a loss of multifractality has been associated with impaired regulatory complexity [6]. In markets, temporal variation of multifractal descriptors has been studied in relation to changing market conditions and efficiency [8]. These examples support the use of multifractal quantities as state-sensitive observables, provided that the interpretation follows from the dynamics of the system and from the robustness of the estimated spectrum.

### *5.3. Criticality and Regime Transitions*

Critical phenomena provide a particularly demanding setting for this interpretive step because scale invariance, heavy tails, long-range correlations, and multifractality can coexist without being equivalent indicators of the same mechanism. Self-organized criticality (SOC) was introduced to describe dynamical systems that can evolve toward a critical state without external tuning [68]. Multifractal spectra can enrich this description by resolving heterogeneous scaling within the observed fluctuations, although the spectrum alone does not identify an SOC mechanism. Likewise, empirical power laws require explicit estimation of the scaling range, goodness-of-fit testing, and comparison with plausible alternatives [69]. Evidence for criticality is stronger when scaling, temporal dependence, clustering, and multiscale organization are examined jointly and when alternative statistical explanations remain visible.

The long-term study of blackouts in China's power system published in this Special Issue provides a useful example of such a combined strategy [70]. The authors analyze event sizes and inter-event intervals over the period 1981–2025 through power-law fitting, several Hurst-exponent estimators, symbolic dynamics, and MF-DFA. Their results identify persistent temporal dependence and a broad singularity spectrum, while shuffling experiments attribute a substantial component of the multifractal width to the temporal organization of the sequence. The power-law hypothesis is evaluated through maximum-likelihood fitting, goodness-of-fit testing, and comparisons with alternative heavy-tailed models, and the authors interpret the resulting profile as consistent with SOC dynamics [70]. Within the framework developed in this review, the study is informative because the multifractal result forms one component of a broader evidential profile. That convergence strengthens the SOC interpretation without making it a unique mechanistic identification.

The same logic applies more generally to regime transitions in complex systems. Multifractal observables can be sensitive to reorganizations that change how fluctuations are distributed across scales, making them useful candidates for comparative analysis across operating conditions, developmental stages, or dynamical phases. Their diagnostic value increases when the observed changes can be connected to independently established modifications of coupling, constraints, or control structure. This perspective positions

multifractality as a probe of organized variability by compressing heterogeneous scaling into quantities that can be compared across states while preserving the need for domain-specific evidence when those quantities are used to infer memory, criticality, or mechanism. The next sections extend this logic to changes in the support itself, first through spatial growth and complex networks and later through computational representations and learning systems.

## 6. Changing the Support: Spatial Systems and Complex Networks

The meaning of a multifractal description becomes more explicit when the support is no longer a one-dimensional temporal record. Spatial growth processes and complex networks require the analyst to specify how mass is distributed, how distance is measured, and how scale is constructed before any generalized dimension can be interpreted. This shift provides a useful test of the organizational notation introduced in Equation (15), because changes in $\mathcal{S}$, $\mu$, or $\rho$ alter the object to which the multifractal statement refers even when the estimator retains a familiar mathematical form. Spatial aggregates illustrate the distinction between fractal geometry and multifractal heterogeneity, while networks make the dependence on metric and support construction unavoidable.

### *6.1. Spatial Growth and Fractal Organization*

Diffusion-limited aggregation (DLA) is a canonical example of a stochastic growth process that generates irregular, self-similar structures. Particles diffuse until they attach to an existing cluster, producing branched morphologies whose geometry can be summarized through a box-counting dimension [71]. The study by Salcedo-Sanz et al. [72] in this Special Issue extends this construction through seeded DLA and concentration-gradient diffusion, using pre-existing fractal structures—including strange attractors, iterated-function-system patterns, Lindenmayer-system structures, and percolation-based clusters—as condensation nuclei. The resulting aggregates are characterized primarily through the box-counting dimension, allowing the authors to quantify how the initial geometry and subsequent aggregation modify the effective spatial complexity of the cluster.

This setting is useful for clarifying the boundary between fractal and multifractal characterization. A box-counting dimension summarizes how the number of occupied boxes scales with their linear size,

$$N(\epsilon) \sim \epsilon^{-D_{\mathrm{B}}}, \tag{17}$$

where $N(\epsilon)$ is the number of boxes of size $\epsilon$ required to cover the aggregate and $D_{\mathrm{B}}$ is the box-counting dimension. The estimate captures a global scaling relation and is therefore well suited to comparing the overall geometry of different aggregates. A multifractal analysis requires an additional measure distributed over the support and examines how regions carrying different amounts of that measure scale across resolutions. In the language of Equation (15), the support supplied by the aggregate is sufficient for a fractal analysis, while a multifractal description additionally requires an explicit choice of $\mu$ whose heterogeneity is scientifically meaningful.

The seeded-DLA results also illustrate how growth processes can retain or progressively transform information inherited from an initial structure. Small aggregation radii preserve more of the seed morphology, whereas larger radii allow the stochastic DLA dynamics to dominate the final geometry [72]. The phenomenon can be interpreted as a competition between inherited spatial organization and growth-induced restructuring. Its relevance here is conceptual because the scaling properties of a complex object depend jointly on the support produced by the dynamics and on the observable selected to quan-

tify that support. This distinction prepares the transition to networks, where even the construction of distance is part of the analysis.

### *6.2. Multifractality on Networks*

In complex networks, Euclidean proximity is replaced by relational structure, and Song et al. [73] showed that several real networks exhibit self-similarity under a box-covering renormalization in which nodes are grouped into boxes whose members lie within a prescribed graph distance. Subsequent work developed and compared box-covering and edge-covering algorithms, making the computational construction of graph scale itself an object of methodological study [74–76]. This result established that the small-world character of many networks does not preclude fractal organization and provided a basis for treating graph distance as a scale variable. The corresponding support is the node set together with its connectivity, while the radius or diameter of a graph neighborhood supplies the operational notion of scale.

Furuya and Yakubo [9] extended this perspective to multifractality by showing that structural measures on several deterministic, stochastic, and real-world fractal scale-free networks yield nonlinear mass exponents $\tau(q)$. Their analysis associates multifractal behavior with strong fluctuations in local node density, thereby translating the classical idea of heterogeneous mass distribution into a topological setting. The resulting object is a topological measure induced by how nodes populate graph neighborhoods across scales, rather than a geometrical density defined directly in Euclidean space.

Sandbox methods provide an efficient implementation of this idea by selecting a node $v$ as the center of a graph neighborhood of radius $r$ and defining $M_v(r)$ as the mass contained within that neighborhood. Fixed-mass formulations provide a complementary construction and have been developed both for direct network measures and for sandbox sampling [77,78]. Repeating the construction over many centers gives access to moments of the form

$$\left\langle M_v(r)^{q-1} \right\rangle \sim \left(\frac{r}{d}\right)^{(q-1)D_q}, \qquad q \neq 1, \tag{18}$$

where $\langle \cdot \rangle$ denotes an average over sandbox centers, $d$ is the network diameter, and $D_q$ is the generalized dimension of order $q$. The information dimension $D_1$ requires the corresponding logarithmic limit. Liu et al. compared this approach with compact-box-burning and improved box-counting procedures and found the sandbox formulation effective for estimating mass exponents across several model networks [35]. Weighted extensions subsequently replaced purely topological distance or node count with quantities that incorporate edge weights, expanding the possible definitions of both scale and mass [36].

The expanding network literature also shows that multifractal estimates can track temporal network growth, environmental visibility graphs, and directed connectivity [79–81]. The role of geometry becomes even clearer in spatially embedded networks. Rak and Rak [37] introduced a geometric sandbox algorithm that incorporates node coordinates in addition to connectivity and showed that the inferred multifractal structure can change when geometric information is included. The result has a direct methodological implication because network multifractality is conditional on the metric structure used to define neighborhoods. Two analyses performed on the same adjacency graph can answer different scientific questions when one uses shortest-path distance and another uses physical embedding.

Figure 9 isolates this dependence in a controlled benchmark in which the adjacency matrix is held fixed while only the planar embedding is changed. The reference topology is a $16 \times 16$ grid graph with $N = 256$ nodes. The three geometry classes comprise an approximately aligned grid, a four-cluster embedding, and a nonlinear radial warp. For each class, 16 independently perturbed embeddings are analyzed over $q \in [-2, 2]$. The

standard sandbox uses shortest-path distance and therefore returns the same generalized-dimension profile $D_q$ for every embedding. The geometric sandbox follows the geometry–connectivity construction of Rak and Rak [37], in which a Euclidean neighborhood supplies the candidate nodes while the mass is restricted to the connected component containing the sandbox center within the induced subgraph. All nodes are used as sandbox centers.

The scale normalization depends on the metric. In the standard topological sandbox, $d$ in Equation (18) denotes the graph diameter in shortest-path distance. For the geometric-sandbox benchmarks, a Euclidean radius $R$ is instead normalized as $\rho = R/P$, where $P = \max_{u,v \in V} \|\mathbf{x}_u - \mathbf{x}_v\|_2$ is the Euclidean diameter of the node embedding, computed separately for each realization. The topological and geometric diameters are therefore distinct normalization quantities.

The upper-right panel shows that changing the embedding modifies the geometry-sensitive $D_q$ profile even though the graph topology is unchanged. To summarize this effect, define $\Delta D = D_{q_{\min}} - D_{q_{\max}}$ with $q_{\min} = -2$ and $q_{\max} = 2$. Across the 16 realizations, the median geometric-sandbox values are approximately 0.026, 0.107, and 0.182 for the aligned, clustered, and radial-warp embeddings, respectively. The lower-right panel reports the shift of these class medians relative to the aligned geometry, so the aligned value is zero by construction and the clustered and radial-warp shifts are approximately 0.081 and 0.157. The ordering aligned $<$ clustered $<$ radial warp is preserved under three tested geometric-radius windows for this $N = 256$ configuration, while the median coefficients of determination for the scaling fits remain above 0.98 in every geometry class. The benchmark therefore illustrates a support-construction effect rather than a change in adjacency. Geometry enters the scale rule $\rho$ and changes the multifractal object on which the estimator acts.

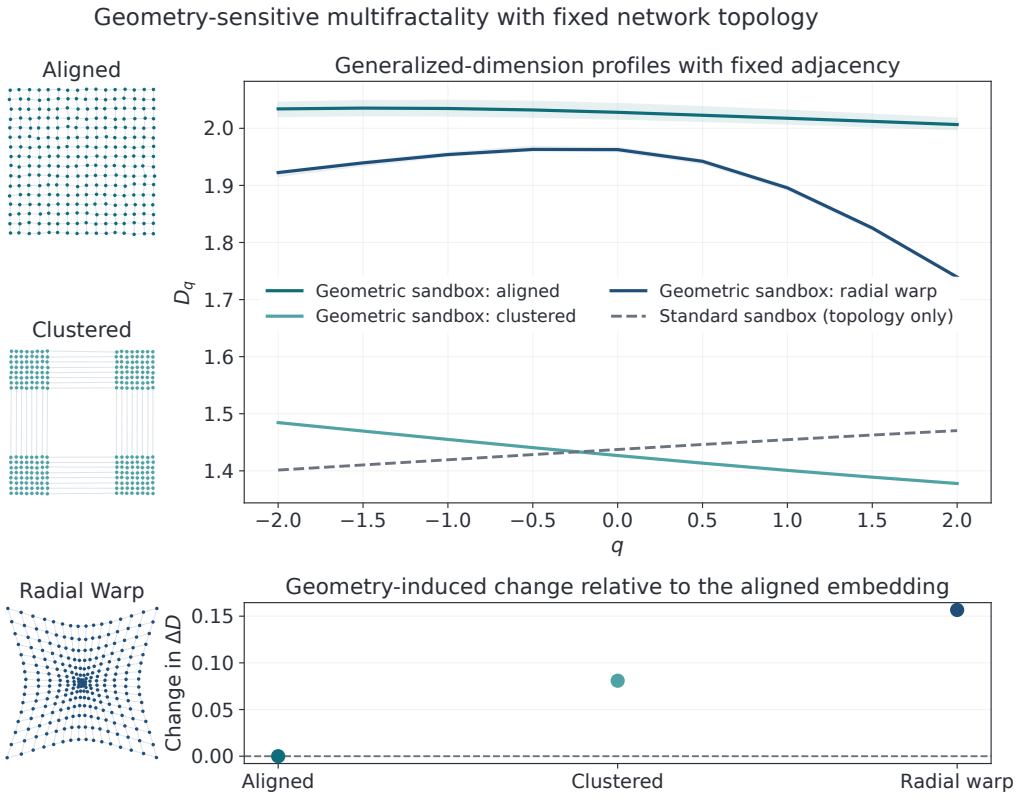


**Figure 9.** Controlled benchmark of geometry-sensitive multifractality at fixed network topology. The three panels on the left show different planar embeddings of the same $16 \times 16$ grid adjacency graph. The upper-right panel compares generalized-dimension profiles $D_q$ for the standard sandbox, which uses shortest-path distance and is therefore invariant to the embedding, with geometric-sandbox profiles obtained from aligned, clustered, and radially warped embeddings. Curves for the geometric sandbox summarize 16 independently perturbed embeddings per geometry class over $q \in [-2, 2]$. The lower-right panel reports the change in the class-median $\Delta D = D_{q_{\min}} - D_{q_{\max}}$ relative to the aligned embedding. The aligned value is therefore zero by construction, while positive values quantify the additional geometry-sensitive spread produced by the clustered and radial-warp embeddings. The benchmark follows the geometry–connectivity principle of the geometric sandbox algorithm and is included to illustrate that multifractal inference on networks depends on the metric and scale construction even when adjacency is held fixed.

To expose the scaling relations underlying the geometric-sandbox estimates, define the finite-scale moment ordinate $S_q(\rho)$ for a sandbox mass $M_v(\rho)$, with $\rho = R/P$ denoting the normalized geometric radius defined above. Its fitted slope against $\log \rho$ yields the estimated generalized dimension $D_q$, including the logarithmic $q = 1$ limit:

$$S_q(\rho) = \begin{cases} \dfrac{\log \langle M_v(\rho)^{q-1} \rangle}{q-1}, & q \neq 1, \\ \langle \log M_v(\rho) \rangle, & q = 1. \end{cases} \qquad D_q \approx \frac{\mathrm{d}S_q(\rho)}{\mathrm{d}\log \rho}. \tag{19}$$

Figure 10 displays these functions for $q = -2, 0, 1, 2$ and each of the three embeddings in the original $N = 256$ benchmark. Solid curves are medians over 16 realizations, shaded regions give interquartile ranges, and dashed lines indicate fits of the corresponding median curves over the ten normalized radii $\rho \in [0.045, 0.20]$. Although the regressions show approximately linear behavior over the selected radii, this range spans only about 0.65 decades, so a high fit quality alone cannot establish asymptotic multifractal scaling. At the smallest radius, the median fractions of singleton sandboxes are approximately

26.6% and 20.7% for the aligned and radial-warp geometries, respectively; such sparse neighborhoods particularly affect negative moments.

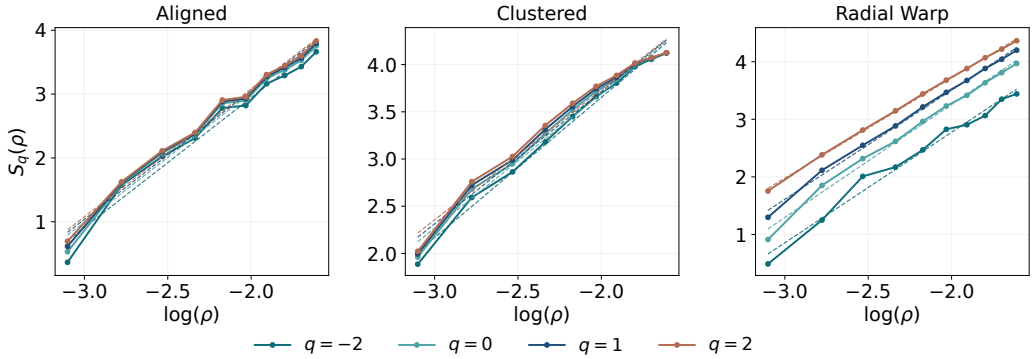


**Figure 10.** Geometric-sandbox scaling diagnostics for the 256-node benchmark of Figure 9. Each panel reports $S_q(\rho)$ for four representative moment orders; solid lines and shaded bands indicate the median and interquartile range across 16 embeddings, and dashed lines are log-radius linear fits to the median curves. The identical interval $\rho \in [0.045, 0.20]$ is used for all three geometries, with radii normalized by the Euclidean embedding diameter $P$.

To assess the role of network size, we repeated the same geometry-sensitive construction on $16 \times 16$, $32 \times 32$, and $64 \times 64$ grid graphs ($N = 256$, 1024, and 4096 nodes), retaining the 16 independently perturbed embeddings per class, all nodes as sandbox centers, $q \in [-2, 2]$, and the same ten normalized geometric radii. Figure 11 shows the resulting finite-size dependence of $\Delta D = D_{-2} - D_2$ and $D_1$. The embedding affects the estimated dimensions at each tested size; however, the ordering of $\Delta D$ across geometry classes is not stable with $N$. For example, the median $\Delta D$ for the radial warp decreases from approximately 0.182 at $N = 256$ to 0.007 and 0.021 at $N = 1024$ and 4096, respectively, while the clustered value changes from 0.107 to 0.137 and 0.144. The aligned configuration yields negative estimated $\Delta D$ at the two larger sizes, a departure from the expected monotonic ordering of generalized dimensions that further indicates sensitivity to finite-scale estimation. Thus, the original benchmark isolates the dependence on geometric neighborhood construction at fixed adjacency, but its numerical width rankings must not be extrapolated to other network sizes or interpreted as converged multifractal characteristics.

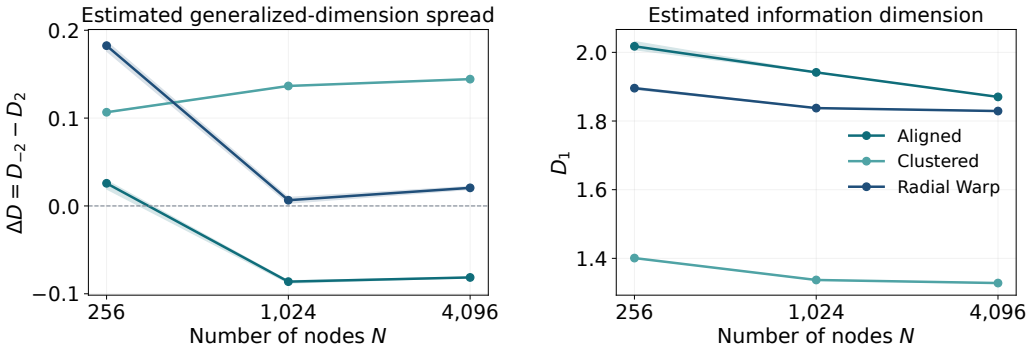


**Figure 11.** Finite-size sensitivity of geometric-sandbox estimates on $N = 256$, 1024, and 4096 node grids. Left: $\Delta D = D_{-2} - D_2$; right: the information-dimension estimate $D_1$. Markers represent medians across 16 realizations for each network size and embedding, with shaded interquartile ranges. All estimates use the same ten radii normalized by the embedding-specific Euclidean diameter $P$ and the same moment range, and are interpreted as finite-scale numerical descriptors rather than asymptotic dimensions.

Geometric information need not be limited to physical coordinates. Hyperbolic geometry provides a natural latent space for many complex networks: when nodes are placed in a hyperbolic space and connected according to their hyperbolic distances, heterogeneous degree distributions and strong clustering emerge as reflections of the negative curvature and metric property of the space, and, conversely, a heterogeneous network with a metric structure has an effective hyperbolic geometry underneath [82]. Ren et al. [38] embedded networks in hyperbolic space, used the resulting geometric information to assign weights to the edges of the original network, and analyzed the reconstructed networks with the sandbox algorithm for weighted networks, so that inter-node distances combine topological and geometric information. Across model networks, computational mesh networks, and real-world networks, the introduction of geometric information changed the generalized dimensions to varying degrees, and the interplay between topology and geometric weight assignment was found to regulate the emergence of multiscale complexity [38]. Hyperbolic geometry has also been examined from a dynamical perspective in growing networks, where MF-DFA applied to metrics of the local topological and geometric perturbations induced by each newly added node in the hyperbolic popularity–similarity optimization model revealed parameter-dependent multifractality, with similar properties observed in a real Autonomous System network [83]. In the notation of Equation (15), these approaches show that the geometry entering the scale construction $\rho$ may be physical or latent, and in either case, it becomes part of the multifractal object on which the estimator acts.

Network analysis therefore makes explicit a principle that remains relevant throughout the rest of this review. Multifractality is attributed to an object only after the support, the distributed measure, and the scale construction have been specified. The estimator acts on this constructed object and cannot supply those modeling choices by itself. This point becomes especially important for learning systems, where candidate supports include parameters, neurons, interaction graphs, hidden representations, and loss landscapes. The transition from networks to artificial intelligence thus preserves the same mathematical question while enlarging the set of admissible loci on which multifractal organization can be defined.

The estimator alternatives collected in Supplementary Table S1 further distinguish changes of estimator on a fixed network object from changes in the metric or neighborhood rule used to define that object.

## 7. From Multifractal Signatures to Computational Representations

The role of multifractal analysis changes when quantities extracted from a signal, image, or symbolic sequence are used as inputs to a predictive or discriminative model. The singularity spectrum then serves as a compact representation of the original object rather than solely as a description of multiscale organization. Let $X$ denote the observation and $\mathcal{M}$ the multifractal analysis defined by the choices summarized in Equation (15). Applying $\mathcal{M}$ to $X$ yields a descriptor vector $z_{\mathrm{MF}}$, which a statistical or machine-learning model $g$ uses to produce an estimate $\widehat{y}$. The scientific question concerns how much target-relevant information remains encoded in $z_{\mathrm{MF}}$ and whether that information generalizes beyond the sample used to construct the representation.

A multifractal representation may contain the spectrum width $\Delta\alpha$, its location and asymmetry, selected generalized dimensions, values of $h(q)$, or combinations of these quantities. Such features summarize relationships that are distributed across many temporal or spatial scales and can therefore complement local statistics or frequency-domain descriptors. Their compactness is attractive when the downstream model must operate on heterogeneous data with limited sample size, although the compression also removes information. A classifier trained on $\Delta\alpha$ or a small set of singularity-spectrum parameters

does not observe the original sequence and cannot recover distinctions that the chosen multifractal map has discarded. Feature design consequently determines which aspects of multiscale organization remain accessible to learning.

Biomedical signal analysis provides an early concrete illustration of this representational use within a broader literature on fractal and multifractal features for medical pattern recognition, texture analysis, and segmentation [23]. Zhang et al. [84] extracted eight multifractal-spectrum features from intracranial electroencephalographic recordings and used them as inputs to a relevance vector machine for seizure detection. The approach treats the spectrum as a feature-generating transform, while discrimination between interictal and ictal states is delegated to a supervised model whose input consists of parameters describing local singularity structure. Comparable pipelines have been developed across biomedical applications in which multifractal quantities are combined with conventional statistical or spectral features [23,84]. The same strategy also exposes a limitation identified by França et al. [85], who showed that fractal and multifractal descriptors of electrographic recordings can correlate strongly with signal variance, demonstrating that an apparently sophisticated scaling feature may encode a simpler property of the signal unless confounding factors are explicitly examined. Representation quality therefore depends on both predictive performance and evidence that the extracted quantities capture the intended structure.

A comparable transition from diagnosis to representation occurs in symbolic data, as the study discussed in Section 5 used multifractal descriptors derived from morphologically mapped texts for pattern recognition across languages [66]. The relevant change of role is conceptual because the same spectrum that supports an interpretation of long-range morphological organization also becomes a coordinate system in which different linguistic objects can be compared computationally. A later study extended this strategy to human-written text, machine-generated text, and source code by combining multifractal quantities with recurrence quantification analysis, Zipf-related measures, and other complexity descriptors [10]. The resulting feature space supported classification while preserving a link between the learned decision and interpretable properties of the generated sequences. In both cases, multifractal analysis operates at a mesoscopic level between token-level statistics and a complete model of the generative process.

Two-dimensional data provide a spatial counterpart to this representational strategy. Earlier work used multifractal detrended moving-average quantities for texture representation and image segmentation [86,87], while Wang et al. introduced adaptive multifractal and multifractal cross-correlation methods for complex images and used the resulting descriptors in image-classification tasks, including leaf images and breast-ultrasound data [88]. The reported performance illustrates how heterogeneous texture can be compressed into a small set of scale-dependent characteristics before classification. The methodological contribution is especially relevant because improvements in classification were coupled to changes in the multifractal estimator itself, including adaptive partitioning intended to reduce boundary effects. The example reinforces the connection between representation and evidence developed in Section 4, since gains in downstream accuracy are more informative when the features are also shown to be stable estimates of the intended multiscale structure.

Financial forecasting offers a related use of time-varying multifractal states. Wang and He computed rolling MF-DFA descriptors for USD/KRW exchange-rate returns and augmented an Extra Trees forecasting model with seven scaling features [11]. Their validation design included shuffled, phase-randomized, and IAAFT surrogates, feature ablations, temporal-shift placebos, and out-of-sample evaluation. The reported gains are specific to the studied forecasting problem, which makes the example methodologically useful because multifractal representation can contribute predictive information without imply-

ing that the spectrum provides a universal forecasting variable or a causal description of market dynamics.

Interpreting multifractal features as computational representations requires a feature map that remains valid under the sampling constraints of the data and a predictive contribution isolated through comparison with appropriate non-multifractal baselines and ablations. Preprocessing and rolling estimation must also preserve the temporal or experimental separation between training and evaluation data. The last condition is particularly important for forecasting, because decomposition, normalization, scale selection, or threshold calibration performed on the full record can transfer information from the evaluation interval into the feature construction.

In this representational setting, multifractal information is supplied to the learning algorithm as an externally constructed input description. Section 8 considers architectures in which multifractal quantities enter the computational path itself.

## 8. Computing with Multifractality

The transition from representation to computation occurs when multifractal quantities participate directly in the state-update rules, filtering operations, or adaptive mechanisms of a learning system. The previous section treated multifractal descriptors as externally constructed features, whereas the architectures considered here allow the multifractal transform to influence the internal computation. Current studies exhibit two recurring design patterns. One uses a multifractal descriptor as a complexity-conditioned control signal that modulates memory, gating, or another adaptive component. Another makes the multifractal representation learnable and incorporates it into the end-to-end transformation optimized during training.

A generic complexity-conditioned architecture can be written as

$$c_t = \phi(\mathcal{M}(X_{t-w:t})), \qquad s_t = F_\theta(x_t, s_{t-1}; c_t), \tag{20}$$

where $\mathcal{M}$ extracts a local multifractal descriptor from a window of observations, $\phi$ maps that descriptor to a control variable $c_t$, and $F_\theta$ denotes the state transition of the learning model. The multifractal quantity originates outside the parameterized state transition, while entering the computational path by conditioning how the new state is formed.

The Dynamic Fractal–Chaotic Long Short-Term Memory (DFC-LSTM) architecture provides a clear example of this pattern. Zeng et al. [12] replace the standard forget-gate behavior with a multifractal-driven dynamic gate whose modulation depends on the local spectrum width $\Delta\alpha$. The same architecture introduces a chaos-based dynamic activation, allowing the contributions of the two mechanisms to be examined separately through gate-only and chaos-only ablations. This decomposition is methodologically useful because gate-only and chaos-only ablations provide component-wise empirical evidence about the contribution of the two mechanisms within the reported backtests. In this design, multifractality functions as an adaptive signal governing memory retention in response to changes in the estimated complexity of the input process.

The VMD–MF–GRU model published in this Special Issue, which combines variational mode decomposition (VMD) with a multifractal (MF) gated recurrent unit (GRU), follows a related strategy for financial forecasting [13]. The model estimates time-varying multifractal spectrum widths and uses them to modulate the update mechanism of the GRU. The intended computation links larger local complexity to a change in the retention of historical information. The architecture also includes hidden-state fusion, so the reported performance reflects the combined effect of decomposition, multifractal gating, and state fusion. Moreover, because the two temporary update-gate outputs are individually passed through sigmoid activations and then added, their sum is not constrained to $[0, 1]$. Conse-

quently, the resulting hidden-state update is not guaranteed to remain the conventional convex interpolation between the previous and candidate states [13]. These features make the paper a useful example of multifractality as a computational variable. They also expose the attribution problem discussed in Section 4. The reported state-fusion ablation does not isolate the multifractal gate itself, so the forecasting gains cannot be attributed uniquely to that component.

A stronger form of integration appears when the multifractal transform is itself parameterized and trained within the model. Xiong et al. proposed the Multifractal Spectrum Transformer (MFS-Transformer), which incorporates a learnable three-dimensional multifractal-spectrum estimator together with fractal-domain filtering and iterative learning [14]. The distinction is structural because the model receives no fixed multifractal feature vector produced before training. Instead, the multifractal representation participates in the trainable transformation applied to the input. This construction can be written as

$$z_{\mathrm{MF}} = \mathcal{M}_{\vartheta}(X), \qquad \widehat{y} = G_{\theta}(z_{\mathrm{MF}}), \tag{21}$$

where the multifractal operator carries trainable parameters $\vartheta$ that are optimized jointly with the remaining model parameters $\theta$. Experiments on three-dimensional chaotic systems show that this construction can improve classification under short-sequence and low-signal-to-noise conditions [14]. The current evidence remains concentrated on a restricted class of tasks, so broader claims about general-purpose fractal-domain learning require validation across additional data types and architectures.

Taken together, these examples reveal a gradual change in the computational status of multifractal information. Feature-based approaches use multifractal descriptors to define the representation supplied to an otherwise unchanged learner. Complexity-conditioned architectures move those descriptors into the state dynamics, where an externally estimated measure of complexity modulates memory, gating, or related mechanisms. Learnable multifractal operators place the scaling representation within the trainable computational path itself. These roles form an architectural continuum rather than a sequence of mutually exclusive stages, and a single model may combine elements associated with several positions along that continuum.

Within the literature corpus examined here, evidence for complexity-conditioned and learnable multifractal computation remains comparatively limited, which gives this transition particular relevance for the present review. These studies place multifractal information inside the computational design of a learning system, while the strength of the resulting claims depends on experiments that isolate the multifractal mechanism from accompanying architectural changes. The next section reverses the direction of analysis by treating learning systems themselves as the objects whose internal organization, optimization landscapes, and interaction structures are examined through multifractal methods.

## 9. Learning Systems as Multifractal Objects

The direction of analysis changes once the learning system itself becomes the object whose organization is examined across scales. Multifractal quantities can then refer to several distinct structures generated before, during, or after learning, and these structures should remain separated because they answer different scientific questions. A convenient organization is obtained by distinguishing the complexity of the data, the model, the internal state induced by a specific input, and the output produced by the trained system. We denote these loci as

$$\mathcal{C}_{\mathrm{data}}, \qquad \mathcal{C}_{\mathrm{model}}, \qquad \mathcal{C}_{\mathrm{state}}(x, \ell), \qquad \mathcal{C}_{\mathrm{output}}, \tag{22}$$

where $x$ is an input and $\ell$ indexes computational depth. The notation in Equation (22) labels four loci at which complexity may be studied without assuming that they share a common estimator, unit, or mathematical definition. Across learning-system applications, estimator selection consequently follows the specified analytical locus: a loss landscape, an interaction network, and a generated sequence constitute different objects even when their reported descriptors share the same notation. Supplementary Table S1 records this distinction without assigning a domain-wide preferred estimator. This separation is useful as a model can transform highly structured data into simpler outputs, exhibit a complex optimization landscape while producing regular internal trajectories, or generate outputs whose multifractal organization does not directly reveal the geometry of the trained parameters.

### *9.1. Complexity Loci in Learning Systems*

Among the four loci, $\mathcal{C}_{\text{data}}$ is the closest to established multifractal practice because the data can be analyzed independently of the model that later processes them. The literature reviewed in Sections 5 and 7 belongs largely to this category when multifractal descriptors are computed before learning. The output locus, $\mathcal{C}_{\text{output}}$, shifts attention to structures generated by a trained system. Human–machine text comparisons provide an example in which multifractal and recurrence-based descriptors characterize generated sequences and distinguish output classes [10]. Recursive feedback experiments further show that the statistical organization of generated text can evolve over successive iterations, providing a dynamical view of output complexity [89]. A controlled study of decoder-only Transformers further found that modifying cross-layer connectivity changed long-range structural descriptors of generated text even when perplexity improvements were inconsistent [90]. These analyses reveal properties of the produced sequences while leaving the internal computational path only indirectly constrained.

Model-level complexity, $\mathcal{C}_{\text{model}}$, concerns structures defined by the trained system itself. Depending on the question, the support can be parameter space, a loss landscape, a graph of interactions among units, or another representation derived from the model architecture. The support–measure–scale choices introduced in Section 3 become especially consequential. A loss landscape and a neuron-interaction graph can both exhibit multi-scale heterogeneity, although their generalized dimensions or singularity spectra refer to fundamentally different objects.

The most input-specific locus is $\mathcal{C}_{\text{state}}(x, \ell)$, which refers to the internal representation induced by an input $x$ at layer or computational stage $\ell$. This locus is conceptually distinct from model-level organization because the state depends jointly on the trained parameters and on the particular input being processed. A layer-wise analysis can ask how complexity is transformed through computational depth for different classes of inputs, tasks, or operating regimes. The distinction will become important in the research agenda of Section 10, where internal representations emerge as a comparatively underexplored target for direct multifractal analysis.

### *9.2. Model-Level Multifractality*

An earlier model-level precedent comes from the statistical mechanics of learning. Engel and Weigt showed that random input patterns partition the coupling space of feed-forward neural networks into cells labeled by generated output sequences. For perceptrons, the resulting partition forms a random multifractal whose spectrum can be related to storage and generalization properties [17,18]. Within the present taxonomy, this is naturally interpreted as a model-level construction because the multifractal support is the coupling space rather than an activation trajectory conditioned on a particular input. In the contem-

porary deep-learning literature, loss landscapes provide a direct multifractal construction at the level of the trained system. Ly and Gong introduced a theoretical framework in which deep-learning loss landscapes are modeled as multifractal surfaces with spatially varying Hölder regularity [15]. Their construction reproduces several geometrical features associated with neural-network optimization, including multiscale roughness, clustered degenerate minima, and heterogeneous local curvature. They further derive optimization dynamics that display phenomena such as the edge of stability and nonstationary anomalous diffusion. The study also analyzes two-dimensional sections of empirical neural-network loss landscapes and reports singularity spectra across training stages. Within the present framework, the contribution is significant because the multifractal object is the optimization landscape itself, so the measured heterogeneity belongs directly to $\mathcal{C}_{\text{model}}$.

The explanatory scope of such a model depends on the match between the multifractal construction and the real optimization landscapes to which it is applied. Ly and Gong support this connection through empirical landscape sections and control studies, while the formal mechanism remains a specific theoretical model of loss geometry whose generality across deep networks requires further validation [15]. This distinction mirrors the evidence principles developed in Section 4. A multifractal model can organize several observed phenomena coherently while broader generalization still requires replication across architectures, datasets, optimizers, and definitions of landscape scale.

A second model-level route represents interactions among computational units as a network and analyzes its evolving heterogeneity. NeuroMFA constructs neuron-interaction networks for large models and applies multifractal analysis to their structural organization [16]. The framework is designed to quantify changes in heterogeneity and self-organization and relates the resulting structural measures to model capability. Its locus differs from the loss-landscape approach even though both are properties of the trained system. NeuroMFA defines scale and mass on an interaction network, whereas the loss-landscape formulation defines local regularity over parameter-space sections. Their coexistence demonstrates why $\mathcal{C}_{\text{model}}$ should be understood as a family of model-level objects whose multifractal meaning depends on the chosen support.

### *9.3. Internal Representations as an Open Frontier*

The language of multifractal internal organization also has a historical precedent. In their statistical-mechanics treatment of learning, Engel and Van den Broeck devoted part of their multifractal analysis to the "multifractal organization of internal representations" [91]. That precedent is conceptually important, yet its formal setting belongs to the classical theory of perceptrons, coupling-space partitions, and related internal-representation structures. It should therefore be distinguished from the activation-level object considered here, which is the geometry of hidden states generated by a particular input at a particular computational depth in a contemporary deep or Transformer model. The research gap developed below concerns this latter, input-conditioned locus rather than the first appearance of multifractal ideas in neural learning theory.

The geometry of internal neural representations has already motivated a substantial neighboring literature, including intrinsic-dimension estimators [92], image-representation dimensionality [93], and manifold-based analyses of representational separability [94,95]. Ansuini et al. [96] measured the intrinsic dimension of layer-wise representations in deep networks and reported a characteristic evolution across depth, with dimensionality increasing in early layers and decreasing toward the final hidden representation in the analyzed models. Such results support the broader idea that learning reorganizes representation geometry progressively across layers. Intrinsic dimension, however, is a different object from a multifractal spectrum. A single estimate of dimensionality does not establish a

distribution of local scaling exponents, and a layer-wise dimensionality profile does not by itself imply multifractal organization.

Transformer studies have further shown systematic layer-wise changes in hidden-state geometry and, under in-context learning or supervised fine-tuning, sharp changes in representation structure across depth [97,98]. These results remain adjacent geometric evidence rather than direct evidence of multifractality. Recent methodological work also cautions against assigning a direct ontological meaning to geometric estimators. Schulte and Rügamer show theoretically and empirically that commonly used intrinsic-dimension estimators on neural representations may fail to track the underlying intrinsic dimension that they are assumed to measure [99]. Their result is relevant to multifractal analysis because it exposes the same inferential issue encountered earlier in this review. The numerical behavior of an estimator must be connected carefully to the mathematical property claimed for the representation.

Within the contemporary literature corpus examined here, direct multifractal analysis of input-conditioned hidden states remains much less developed than model-level analysis of loss landscapes or interaction networks. The historical statistical-mechanics antecedents establish that multifractal organization can arise in neural learning spaces, but they do not resolve the activation-level question posed by modern hidden-state geometries. This more specific gap suggests a concrete extension of the present framework. Consider a sequence model with hidden states

$$H^{(\ell)}(x) = \left[\mathbf{h}_1^{(\ell)}(x), \ldots, \mathbf{h}_T^{(\ell)}(x)\right], \tag{23}$$

where $\mathbf{h}_t^{(\ell)}(x)$ denotes the hidden-state vector associated with token position $t$. Given explicit choices of support $\mathcal{S}_\ell$, measure $\mu_\ell$, and scale rule $\rho_\ell$, let $\Psi$ denote the corresponding hypothesis-dependent construction yielding $X^{(\ell)}(x) = \Psi(H^{(\ell)}(x))$. Different choices generally define different multifractal questions. The resulting object can then be compared across layer $\ell$, input $x$, task, and training stage, provided the construction is tied to a precise hypothesis about computation.

Figure 12 summarizes the methodological step required to move from Transformer hidden states to a multifractal characterization. A layer-dependent representation $H^{(\ell)}(x)$ does not determine a unique multifractal object by itself. An explicit choice of support, measure, and scale is first required in order to construct an analyzable observable $X^{(\ell)}(x)$. Multifractal tools can then be applied layer by layer, allowing, where available under the selected formalism, descriptors such as $f_\ell(\alpha)$, $\Delta\alpha_\ell$, $A_{\alpha,\ell}$, $D_{q,\ell}$, and $h_\ell(q)$ to be compared across computational depth. The figure should be read as a research framework rather than as evidence of an established correspondence between Transformer depth and multifractal scale.

Together, these distinctions complete the transition developed across Sections 7–9. Multifractal analysis first summarizes the organization of data, later contributes to representations and model adaptation, and eventually becomes a tool for examining the organization produced by learning itself. The integrative framework developed next uses locus, role, and evidence to keep these uses comparable without collapsing their mathematical differences.

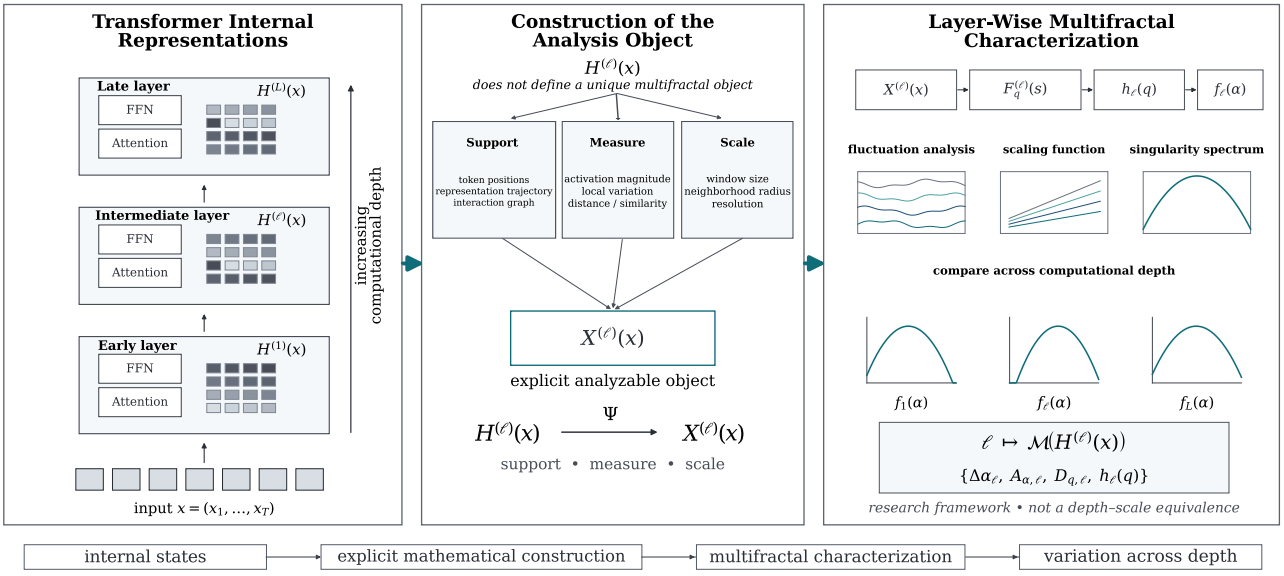


**Figure 12.** Conceptual framework for the multifractal analysis of Transformer internal representations. Given an input $x$, a Transformer produces layer-dependent hidden states $H^{(\ell)}(x)$. A multifractal characterization requires an explicit construction of the analyzed object, including the definition of support, measure, and scale, yielding an observable $X^{(\ell)}(x)$. Standard multifractal tools can then be applied to obtain layer-dependent fluctuation functions, scaling exponents, and singularity spectra $f_\ell(\alpha)$. Comparing these quantities across computational depth provides a possible route for investigating how heterogeneous scaling changes within the model.

## 10. An Integrative Framework and Research Agenda

The preceding sections show that identical multifractal quantities can refer to different scientific objects and serve different inferential purposes. The integrative framework separates three coordinates—locus, role, and evidence—so that contributions can be compared without treating their supports, uses, or evidential requirements as equivalent.

### *10.1. Locus, Role, and Evidence*

The *locus* identifies the object on which the multifractal construction is defined. At the broadest level, the literature considered here spans temporal signals, spatial structures and fields, complex networks, symbolic sequences, and learning systems. The last category can be refined through the four loci introduced in Equation (22), which distinguish data, model-level organization, input-conditioned internal state, and output. This dimension extends the support-centered view introduced in Equation (15), because the interpretation of $D_q$, $\tau(q)$, or $f(\alpha)$ depends on the support and measure from which they are estimated. The same formal quantity can refer to distinct scientific objects when the underlying locus changes.

The *role* specifies what the multifractal quantities are used to accomplish. Five recurrent roles emerge from the corpus. A *descriptor* summarizes heterogeneous scaling without requiring a stronger claim about the mechanism that produced it. A *diagnostic probe* uses the spectrum or generalized exponents to investigate memory, intermittency, regime change, criticality, or another aspect of system organization. A *representation* maps a high-dimensional object into a compact feature space that can support classification, forecasting, or pattern recognition. A *computational variable* participates directly in the state updates, filtering operations, or adaptive mechanisms of a learning architecture. Finally, an *endogenous property* refers to multifractality attributed to the learning system itself, as in

loss landscapes or neuron-interaction networks [15,16]. These roles form a design space, and a single study can occupy more than one of them.

The third dimension concerns the evidential basis of a multifractal claim. Section 4 showed that heterogeneous scaling can be supported through several complementary forms of analysis. Let $\mathcal{L}$ and $\mathcal{R}$ denote, respectively, the locus and role families described above, and define the universe of evidence dimensions as

$$\mathcal{D}_E = \{\text{scal}, \text{unc}, \text{surr}, \text{FS}, \text{cross}, \text{mech}\}, \qquad E_i \subseteq \mathcal{D}_E, \tag{24}$$

where the tags denote scaling evidence, uncertainty analysis, surrogate-based source discrimination, finite-size or finite-length assessment, cross-method validation, and mechanistic or source-level support. The evidence profile records which dimensions are directly supported for study $i$ and does not define a scalar quality index. Different research settings can support different subsets. A theoretical construction may provide mechanistic grounding while making surrogate analysis irrelevant, whereas an empirical time series may provide strong surrogate and uncertainty evidence without yielding a complete generative model.

Because a study can occupy more than one locus or scientific role, we allow $L_i \subseteq \mathcal{L}$ and $R_i \subseteq \mathcal{R}$ and represent each contribution as

$$P_i = (L_i, R_i, E_i). \tag{25}$$

Singleton sets recover the common case in which a dominant locus or role is sufficient. Table 3 applies this organization to representative works discussed throughout the review.

**Table 3.** Representative and boundary works mapped to the Locus–Role–Evidence framework. The evidence profile summarizes the controls or arguments most relevant to interpretation and is not a numerical quality score.

| Representative Work | Locus | Role | Evidence Profile and Interpretive Use |
|---|---|---|---|
| Halsey et al. [3] | Spatial structure | Descriptor | **Scaling.** Generalized dimensions, mass exponents, and the singularity spectrum formalize heterogeneous scaling on fractal supports. |
| Kantelhardt et al. [5] | Temporal signal | Descriptor; diagnostic probe | **Scaling; Surrogates; Cross-method.** MF-DFA, its partition-function correspondence, and shuffled controls discriminate correlation- from distribution-driven signatures. |
| Ivanov et al. [6] | Temporal signal | Diagnostic probe | **Scaling; Surrogates.** Shuffled and Fourier-phase-randomized controls link heartbeat multifractality to nonlinear temporal organization; congestive heart failure shows a marked loss. |
| Kwapień et al. [19] | Temporal signal | Diagnostic probe | **Scaling; Finite-size; Mechanistic.** Analysis and simulation show length-dependent apparent multifractality in uncorrelated series and tie genuine multifractality, within the studied MF-DFA setting, to temporal correlations. |
| Kluszczyński et al. [20] | Temporal signal | Diagnostic probe | **Scaling; Mechanistic.** Controlled cascades preserve correlations while tail thickness is tuned, isolating how distributional properties modulate spectrum span. |

**Table 3.** *Cont.*

| Representative Work | Locus | Role | Evidence Profile and Interpretive Use |
|---|---|---|---|
| Jaroszewicz et al. [21] | Spatial structure | Diagnostic probe | **Scaling; Finite-size.** Finite-size scaling shows broad apparent spectra in the analyzed Ising settings contracting toward zero width in the thermodynamic limit. |
| Song et al. [73] | Network | Descriptor | **Scaling (boundary fractal case).** Box-covering renormalization establishes network self-similarity; the study is retained as a fractal boundary case, not a full multifractal analysis. |
| Furuya and Yakubo [9] | Network | Descriptor | **Scaling.** Analytical and numerical nonlinear mass exponents $\tau(q)$ support multifractal organization in fractal scale-free networks. |
| Rak and Rak [37] | Network | Descriptor; diagnostic probe | **Scaling; Cross-method.** Standard and geometry-aware sandbox analyses show that inferred multifractal structure depends on network geometry and embedding. |
| De Santis et al. [66] | Symbolic sequence | Representation; diagnostic probe | **Scaling; Cross-method.** Multifractal and long-range descriptors, multivariate statistics, and machine-learning validation support morphological characterization and discriminative representation. |
| De Santis et al. [10] | Symbolic sequence | Representation | **Scaling; Cross-method.** MF-DFA, recurrence, Zipf-law, entropy, multivariate, and classification analyses jointly support complexity-based discrimination of human, machine-generated, and code-like text. |
| De Santis et al. [89] | Symbolic sequence | Diagnostic probe | **Scaling; Cross-method.** Multifractal and long-range measures combined with semantic and syntactic indicators support degradation of lexical organization across recursive generations. |
| Salcedo-Sanz et al. [72] | Spatial structure | Descriptor | **Scaling (boundary fractal case).** Box-counting characterizes seeded DLA and diffusion-generated aggregates; the study is retained as a fractal rather than full multifractal case. |
| Yu et al. [70] | Temporal signal | Diagnostic probe | **Scaling; Uncertainty; Surrogates; Cross-method.** Power-law, Hurst, symbolic, MF-DFA, bootstrap/significance, and shuffled controls support long-range and multifractal organization compatible with, but not uniquely proving, SOC. |
| Xiong et al. [14] | Learning system | Computational variable | **Scaling.** A learnable multifractal spectrum and fractal-domain filtering establish computational integration; predictive gains are kept separate from causal attribution. |
| Li [13] | Learning system | Computational variable | **Scaling.** Spectrum width from the decomposed series modulates the GRU update mechanism, establishing architectural use without isolating it as the cause of forecasting gains. |
| Ly and Gong [15] | Learning system | Endogenous property | **Scaling; Mechanistic.** A theoretical multifractal loss-landscape model is linked to optimization dynamics and checked against deep-learning landscape geometry. |
| Xiao et al. [16] | Learning system | Endogenous property | **Scaling.** Neuron-interaction networks are analyzed across model scale and training; the emergence metric is treated as a structural proxy rather than causal evidence. |

The framework also clarifies how scientific use broadens across Sections 5–9, from the analysis of structure and dynamics toward representation, computation, and learning systems. Equation (25) supplies the analytical coordinates needed to compare contributions that occupy different positions within this broader landscape.

This separation also allows the methodological support available for each role and locus to be examined explicitly. Network multifractality requires sensitivity to graph distance, mass definition, and geometric embedding [37]. Time-series studies require attention to finite length, temporal correlations, and surrogate construction [19,20]. Learning-system studies require experimental designs capable of isolating architectural contributions and distinguishing model-level from input-conditioned complexity.

Table 4 complements the role-based comparison above by reorganizing the learning-system literature according to the four complexity loci introduced in Section 9. It distinguishes multifractal structure measured in data, model-level objects, input-conditioned internal states, and outputs without repeating the Locus–Role–Evidence classification.

**Table 4.** Multifractality across learning-system complexity loci. The rows distinguish where complexity is measured and summarize the type of evidence represented in the reviewed corpus; the loci are analytical distinctions and need not be mutually exclusive within a single learning pipeline.

| Complexity Locus | Analyzed Object or Support | Representative Evidence in the Reviewed Corpus | Interpretive Status |
|---|---|---|---|
| $\mathcal{C}_{\text{data}}$ | Input or training signals and multifractal descriptors derived from them | Rolling or local multifractal descriptors are used as predictive representations or control signals in forecasting architectures [11–13]. | Direct input-side characterization and computational reuse; these analyses do not by themselves establish multifractality of the learned model or its hidden states. |
| $\mathcal{C}_{\text{model}}$ | Model-level objects such as coupling-space partitions, optimization landscapes, and neuron-interaction networks | Classical statistical-mechanics work established multifractal coupling-space partitions in perceptrons and feedforward networks [17,18]; recent studies analyze loss landscapes and neuron-interaction networks [15,16]. | Direct endogenous model-level analysis across historically distinct constructions, with interpretation tied to the specific support on which the multifractal measure is defined. |
| $\mathcal{C}_{\text{state}}(x, \ell)$ | Input-conditioned hidden representations or trajectories across computational depth | Historical statistical-mechanics treatments discussed multifractal internal representations in classical neural learning theory [91], whereas the contemporary corpus contains much less direct multifractal evidence on activation-level hidden-state geometries. Neighboring studies establish that representation geometry changes with depth and that geometric estimators require careful interpretation [96,99]. | This remains an explicit open frontier because the historical precedent does not determine a multifractal construction for modern input-conditioned hidden states. Support, measure, and scale must be defined before layer-wise comparison is meaningful. |
| $\mathcal{C}_{\text{output}}$ | Generated symbolic sequences or recursively generated outputs | Complexity and multifractal descriptors characterize generated text and changes induced by recursive feedback [10,89]. | Direct output characterization; an output spectrum does not by itself identify the scaling organization of the internal states that produced it. |

### *10.2. Research Gaps Emerging from the Framework*

Causal interpretation remains unresolved because a broad singularity spectrum can be compatible with several generating mechanisms, including multiplicative cascades, hetero-

geneous correlations, intermittent dynamics, and finite-size effects. Source-discrimination procedures constrain this ambiguity, although they rarely identify a unique mechanism. Progress in this direction requires studies in which multifractal observables are paired with interventions, controlled generative models, or independently measurable dynamical variables. The objective is to establish which changes in system organization produce reproducible changes in the spectrum and which spectral properties remain non-identifiable from observational data alone.

Cross-method and cross-domain comparability presents a related challenge, since the outputs of mature estimators still depend on moment range, scale selection, detrending, measure definition, graph metric, and geometric embedding [22,37]. Comparisons of $\Delta\alpha$, $D_q$, or related summaries across studies require explicit reporting of these construction choices. Shared benchmark datasets and analysis protocols would help distinguish differences caused by the underlying system from those introduced by the estimator, especially in networks and learning systems where scale admits several plausible definitions.

Finite-size robustness is equally central because spectral broadening can contract with increasing sample length or system size and can depend strongly on the selected moment range [19,21,40]. When inference rests on a single spectrum from one record or realization, replication across realizations, subjects, temporal windows, or model initializations can establish whether the inferred multifractality is stable at the ensemble level. Reporting confidence intervals for spectrum-derived quantities would also improve comparisons across conditions and reduce the interpretive weight placed on small differences in $\Delta\alpha$.

The computational use of multifractality introduces a related attribution problem. When multifractal features or gates are embedded in larger architectures, improvements in prediction or classification can arise from several simultaneous changes. The examples reviewed in Sections 7 and 8 show that ablations, matched baselines, temporally appropriate control experiments, and leakage-safe evaluation are essential for identifying the multifractal contribution. Future architectures can strengthen this evidence by comparing fixed, adaptive, and learnable representations under the same training protocol.

The expansion toward learning systems creates a broader conceptual gap around internal representations. Historical statistical-mechanics work already established multifractal coupling-space partitions in perceptrons and feedforward networks [17,18], and later synthesized this line of analysis under an explicit discussion of the multifractal organization of internal representations [91]. These antecedents concern classical learning-theory constructions and should be distinguished from direct multifractal analysis of activation-level hidden states generated by a specific input in a contemporary deep model. Recent work has extended model-level multifractal analysis to loss landscapes and neuron-interaction networks [15,16]. The layer-wise geometry of hidden representations is also known to evolve through computational depth, as shown in intrinsic-dimension analyses of deep networks and Transformers [96,97], while recent work cautions that geometric estimators may fail to track the theoretical quantity they are assumed to measure [99]. As summarized in Table 4, the contemporary literature examined here contains much less direct evidence concerning multifractal organization of input-conditioned hidden states. This historically qualified imbalance identifies $\mathcal{C}_{\text{state}}(x, \ell)$ as a concrete target for future investigation.

The next step at this locus is comparative rather than definitional. Once a hidden-state observable and its support–measure–scale construction have been fixed, studies should test whether layer-wise multifractal changes replicate across architectures, tasks, training stages, and input classes, and whether those changes are systematically related to transformations observed at the output locus. Such designs would help distinguish architecture-specific effects from recurrent properties of learned representation dynamics.

The framework developed here also suggests a broader program for complex-systems research. Multifractality can serve as a bridge between observable structure and computation when its locus, role, and evidence remain explicit. Progress will depend on stronger separation between statistical signature and mechanism, greater comparability across estimators, and experimental designs that expose how scaling organization changes under controlled perturbations. These requirements provide a common basis for evaluating established applications and emerging learning-system studies within the same conceptual structure.

## 11. Conclusions

Multifractal analysis has developed from a mathematical framework for heterogeneous scaling into a broader language for investigating organization across complex systems. Its scientific role now spans the description of scale-dependent structure, the diagnosis of memory and dynamical regimes, the construction of compact representations, the modulation of learning algorithms, and the analysis of learning systems themselves. This expansion increases the explanatory reach of multifractal methods while also making their interpretation more dependent on the object being measured and on the evidence supporting the resulting claims.

The review has treated multifractality through three complementary dimensions organized around locus, role, and evidence. Locus specifies where scaling heterogeneity is defined, role describes how multifractal quantities are used, and the evidence profile records which controls and arguments support the interpretation. This organization makes it possible to compare studies across temporal signals, spatial structures, networks, symbolic systems, and learning architectures without collapsing their mathematical differences.

Broad singularity spectra can reflect persistent multiscale organization, finite-size effects, distributional heterogeneity, temporal correlations, estimator choices, or combinations of these factors. The strength of a multifractal interpretation depends on making explicit the evidence dimensions relevant to the scientific question, including scaling stability, uncertainty, surrogate analysis, finite-size behavior, cross-method agreement, and mechanistic knowledge. The distinction between apparent and supported multifractality provides a practical way to preserve the descriptive value of observed scaling while calibrating stronger dynamical or mechanistic interpretations.

The emerging interaction with machine learning extends this logic in two directions. Multifractal quantities can become computational resources when they are used as representations, adaptive control variables, or trainable components. Learning systems can also become the objects of multifractal analysis through loss landscapes, interaction networks, outputs, and potentially input-conditioned hidden representations. Among these loci, the multifractal organization of input-conditioned hidden representations remains comparatively underexplored and provides a concrete direction for testing how heterogeneous scaling changes through computational depth.

The continued development of multifractal methods will depend on tighter links between mathematical definition, estimator behavior, experimental design, and mechanism. Stronger finite-size controls, shared benchmarks, explicit ablations, and carefully defined supports and measures can improve comparability across domains. Within such a framework, multifractality retains its value as a compact description of complex organization while gaining a clearer role as a bridge between observed structure, dynamics, representation, and computation.

**Supplementary Materials:** The following supporting information can be downloaded at https://www.mdpi.com/article/10.3390/fractalfract10110747/s1, Supplementary File S1 provides the benchmark code, data, and reproducibility documentation; Supplementary File S2 provides Sup-

plementary Table S1, a domain-oriented comparison of multifractal estimators and methodological alternatives.

**Author Contributions:** Conceptualization, E.D.S.; methodology, E.D.S.; software, E.D.S.; validation, E.D.S.; formal analysis, E.D.S. and A.M.; investigation, E.D.S.; data curation, E.D.S.; writing—original draft preparation, E.D.S. and A.M.; writing—review and editing, E.D.S., A.M., and A.R.; visualization, E.D.S. All authors have read and agreed to the published version of the manuscript.

**Funding:** This research received no external funding.

**Data Availability Statement:** The review does not introduce a new empirical dataset. Synthetic series and measures used in the explanatory benchmarks are generated procedurally from the models described in the text. The reproducibility code, random-seed registries, simulation metadata, sensitivity checks, and derived numerical outputs supporting the controlled benchmarks and their scaling, robustness, and finite-size extensions are provided in Supplementary File S1.

**Acknowledgments:** During the preparation of this manuscript, the authors have used ChatGPT (OpenAI, GPT-5.6) for support in preparing explanatory figures (Figures 1, 4 and 12) and as code assistant for the benchmarks. The authors reviewed and edited all outputs and take full responsibility for the content of this publication.

**Conflicts of Interest:** The authors declare no conflicts of interest.

## Abbreviations

The following abbreviations are used in this manuscript:

| | |
|---|---|
| AAFT | Amplitude-adjusted Fourier transform |
| DFC-LSTM | Dynamic fractal–chaotic long short-term memory |
| DLA | Diffusion-limited aggregation |
| DOG | Derivative of Gaussian (order indicated by suffix) |
| GRU | Gated recurrent unit |
| IAAFT | Iterative amplitude-adjusted Fourier transform |
| i.i.d. | Independent and identically distributed |
| MF | Multifractal |
| MF-DFA | Multifractal detrended fluctuation analysis |
| MFS-Transformer | Multifractal spectrum Transformer |
| MRW | Multifractal random walk |
| SOC | Self-organized criticality |
| VMD | Variational mode decomposition |
| VMD–MF–GRU | Variational mode decomposition–multifractal gated recurrent unit |
| WTMM | Wavelet transform modulus maxima |

## References

1. Grassberger, P. Generalized Dimensions of Strange Attractors. *Phys. Lett. A* **1983**, *97*, 227–230. https://doi.org/10.1016/0375-9601(83)90753-3.
2. Hentschel, H.G.E.; Procaccia, I. The Infinite Number of Generalized Dimensions of Fractals and Strange Attractors. *Phys. D Nonlinear Phenom.* **1983**, *8*, 435–444. https://doi.org/10.1016/0167-2789(83)90235-X.
3. Halsey, T.C.; Jensen, M.H.; Kadanoff, L.P.; Procaccia, I.; Shraiman, B.I. Fractal Measures and Their Singularities: The Characterization of Strange Sets. *Phys. Rev. A* **1986**, *33*, 1141–1151. https://doi.org/10.1103/PhysRevA.33.1141.
4. Paladin, G.; Vulpiani, A. Anomalous Scaling Laws in Multifractal Objects. *Phys. Rep.* **1987**, *156*, 147–225. https://doi.org/10.1016/0370-1573(87)90110-4.
5. Kantelhardt, J.W.; Zschiegner, S.A.; Koscielny-Bunde, E.; Havlin, S.; Bunde, A.; Stanley, H.E. Multifractal Detrended Fluctuation Analysis of Nonstationary Time Series. *Phys. A Stat. Mech. Its Appl.* **2002**, *316*, 87–114. https://doi.org/10.1016/S0378-4371(02)01383-3.
6. Ivanov, P.C.; Amaral, L.A.N.; Goldberger, A.L.; Havlin, S.; Rosenblum, M.G.; Struzik, Z.R.; Stanley, H.E. Multifractality in Human Heartbeat Dynamics. *Nature* **1999**, *399*, 461–465. https://doi.org/10.1038/20924.

7. Benzi, R.; Vulpiani, A. Multifractal Approach to Fully Developed Turbulence. *Rend. Lincei. Sci. Fis. Nat.* **2022**, *33*, 471–477. https://doi.org/10.1007/s12210-022-01078-5.
8. Jiang, Z.Q.; Xie, W.J.; Zhou, W.X.; Sornette, D. Multifractal Analysis of Financial Markets: A Review. *Rep. Prog. Phys.* **2019**, *82*, 125901. https://doi.org/10.1088/1361-6633/ab42fb.
9. Furuya, S.; Yakubo, K. Multifractality of Complex Networks. *Phys. Rev. E* **2011**, *84*, 036118. https://doi.org/10.1103/PhysRevE.84.036118.
10. De Santis, E.; Martino, A.; Rizzi, A. Human Versus Machine Intelligence: Assessing Natural Language Generation Models Through Complex Systems Theory. *IEEE Trans. Pattern Anal. Mach. Intell.* **2024**, *46*, 4812–4829. https://doi.org/10.1109/TPAMI.2024.3358168.
11. Wang, D.; He, Y. Multifractal-State-Augmented Machine Learning for One-Trading-Day-Ahead USD/KRW Absolute-Return Forecasting. *Fractal Fract.* **2026**, *10*, 643. https://doi.org/10.3390/fractalfract10090643.
12. Zeng, Y.; Tang, B.; Zhou, Z.; Lee, R.S.T. DFC-LSTM: A Novel LSTM Architecture Integrating Dynamic Fractal Gating and Chaotic Activation for Value-at-Risk Forecasting. *Mathematics* **2025**, *13*, 3587. https://doi.org/10.3390/math13223587.
13. Li, Y. An Improved GRU Financial Time Series Prediction Model. *Fractal Fract.* **2026**, *10*, 227. https://doi.org/10.3390/fractalfract10040227.
14. Xiong, G.; Huang, W.; Zhen, T.; Zhang, S. Fractal-Domain Transformer Based on Learnable Multifractal Spectrum for Chaotic Systems Classification. *Phys. A Stat. Mech. Its Appl.* **2025**, *658*, 130276. https://doi.org/10.1016/j.physa.2024.130276.
15. Ly, A.; Gong, P. Optimization on Multifractal Loss Landscapes Explains a Diverse Range of Geometrical and Dynamical Properties of Deep Learning. *Nat. Commun.* **2025**, *16*, 3252. https://doi.org/10.1038/s41467-025-58532-9.
16. Xiao, X.; Ping, H.; Zhou, C.; Cao, D.; Li, Y.; Zhou, Y.Z.; Li, S.; Kanakaris, N.; Bogdan, P. Neuron-Based Multifractal Analysis of Neuron Interaction Dynamics in Large Models. In Proceedings of the International Conference on Learning Representations, Singapore, 24– 28 April 2025.
17. Engel, A.; Weigt, M. Multifractal Analysis of the Coupling Space of Feedforward Neural Networks. *Phys. Rev. E* **1996**, *53*, R2064–R2067. https://doi.org/10.1103/PhysRevE.53.R2064.
18. Weigt, M.; Engel, A. Multifractality and Percolation in the Coupling Space of Perceptrons. *Phys. Rev. E* **1997**, *55*, 4552–4561. https://doi.org/10.1103/PhysRevE.55.4552.
19. Kwapień, J.; Blasiak, P.; Drożdż, S.; Oświęcimka, P. Genuine Multifractality in Time Series Is Due to Temporal Correlations. *Phys. Rev. E* **2023**, *107*, 034139. https://doi.org/10.1103/PhysRevE.107.034139.
20. Kluszczyński, R.; Drożdż, S.; Kwapień, J.; Stanisz, T.; Wątorek, M. Disentangling Sources of Multifractality in Time Series. *Mathematics* **2025**, *13*, 205. https://doi.org/10.3390/math13020205.
21. Jaroszewicz, S.; Mendez, N.; Beccar-Varela, M.P.; Mariani, M.C. Finite-Size Scaling to Resolve Spurious Multifractality in the Two-Dimensional Ising Model. *Phys. Rev. E* **2026**, *114*, 014139. https://doi.org/10.1103/23vj-5v8c.
22. Salat, H.; Murcio, R.; Arcaute, E. Multifractal Methodology. *Phys. A Stat. Mech. Its Appl.* **2017**, *473*, 467–487. https://doi.org/10.1016/j.physa.2017.01.041.
23. Lopes, R.; Betrouni, N. Fractal and Multifractal Analysis: A Review. *Med. Image Anal.* **2009**, *13*, 634–649. https://doi.org/10.1016/j.media.2009.05.003.
24. Vahab, S.; Sankaran, A. Multifractal Applications in Hydro-Climatology: A Comprehensive Review of Modern Methods. *Fractal Fract.* **2025**, *9*, 27. https://doi.org/10.3390/fractalfract9010027.
25. Rosenberg, E. *A Survey of Fractal Dimensions of Networks*; Springer Briefs in Computer Science; Springer: Cham, Switzerland, 2018. https://doi.org/10.1007/978-3-319-90047-6.
26. Chhabra, A.; Jensen, R.V. Direct Determination of the f(alpha) Singularity Spectrum. *Phys. Rev. Lett.* **1989**, *62*, 1327–1330. https://doi.org/10.1103/PhysRevLett.62.1327.
27. Muzy, J.F.; Bacry, E.; Arneodo, A. Wavelets and Multifractal Formalism for Singular Signals: Application to Turbulence Data. *Phys. Rev. Lett.* **1991**, *67*, 3515–3518. https://doi.org/10.1103/PhysRevLett.67.3515.
28. Muzy, J.F.; Bacry, E.; Arneodo, A. Multifractal Formalism for Fractal Signals: The Structure-Function Approach versus the Wavelet-Transform Modulus-Maxima Method. *Phys. Rev. E* **1993**, *47*, 875–884. https://doi.org/10.1103/PhysRevE.47.875.
29. Kantelhardt, J.W.; Rybski, D.; Zschiegner, S.A.; Braun, P.; Koscielny-Bunde, E.; Livina, V.; Havlin, S.; Bunde, A. Multifractality of River Runoff and Precipitation: Comparison of Fluctuation Analysis and Wavelet Methods. *Phys. A Stat. Mech. Its Appl.* **2003**, *330*, 240–245. https://doi.org/10.1016/j.physa.2003.08.019.
30. Oświęcimka, P.; Kwapień, J.; Drożdż, S. Wavelet versus Detrended Fluctuation Analysis of Multifractal Structures. *Phys. Rev. E* **2006**, *74*, 016103. https://doi.org/10.1103/PhysRevE.74.016103.
31. Jiang, Z.Q.; Zhou, W.X. Multifractal Detrending Moving-Average Cross-Correlation Analysis. *Phys. Rev. E* **2011**, *84*, 016106. https://doi.org/10.1103/PhysRevE.84.016106.
32. Schertzer, D.; Lovejoy, S. Physical Modeling and Analysis of Rain and Clouds by Anisotropic Scaling Multiplicative Processes. *J. Geophys. Res. Atmos.* **1987**, *92*, 9693–9714. https://doi.org/10.1029/JD092iD08p09693.

33. Schmitt, F.; Lavallée, D.; Schertzer, D.; Lovejoy, S. Empirical Determination of Universal Multifractal Exponents in Turbulent Velocity Fields. *Phys. Rev. Lett.* **1992**, *68*, 305–308. https://doi.org/10.1103/PhysRevLett.68.305.
34. Ihlen, E.A.F. Introduction to Multifractal Detrended Fluctuation Analysis in Matlab. *Front. Physiol.* **2012**, *3*, 141. https://doi.org/10.3389/fphys.2012.00141.
35. Liu, J.L.; Yu, Z.G.; Anh, V. Determination of Multifractal Dimensions of Complex Networks by Means of the Sandbox Algorithm. *Chaos* **2015**, *25*, 023103. https://doi.org/10.1063/1.4907557.
36. Song, Y.Q.; Liu, J.L.; Yu, Z.G.; Li, B.G. Multifractal Analysis of Weighted Networks by a Modified Sandbox Algorithm. *Sci. Rep.* **2015**, *5*, 17628. https://doi.org/10.1038/srep17628.
37. Rak, R.; Rak, E. Multifractality of Complex Networks Is Also Due to Geometry: A Geometric Sandbox Algorithm. *Entropy* **2023**, *25*, 1324. https://doi.org/10.3390/e25091324.
38. Ren, H.; Yu, Z.G.; Liu, J.L. Multifractal Analysis of Complex Networks Reconstructed with the Geometric Information from the Embedded Hyperbolic Space. *Chaos Interdiscip. J. Nonlinear Sci.* **2025**, *35*, 053144. https://doi.org/10.1063/5.0271980.
39. Meneveau, C.; Sreenivasan, K.R. Simple Multifractal Cascade Model for Fully Developed Turbulence. *Phys. Rev. Lett.* **1987**, *59*, 1424–1427. https://doi.org/10.1103/PhysRevLett.59.1424.
40. Pamuła, G.; Grech, D. Influence of the Maximal Fluctuation Moment Order q on Multifractal Records Normalized by Finite-Size Effects. *EPL* **2014**, *105*, 50004. https://doi.org/10.1209/0295-5075/105/50004.
41. Zhou, F.X.; Wang, S.; Han, G.S.; Jiang, S.; Yu, Z.G. Randomized Multifractal Detrended Fluctuation Analysis of Long Time Series. *Chaos* **2020**, *30*, 053113. https://doi.org/10.1063/1.5139620.
42. Hu, K.; Ivanov, P.C.; Chen, Z.; Carpena, P.; Stanley, H.E. Effect of Trends on Detrended Fluctuation Analysis. *Phys. Rev. E* **2001**, *64*, 011114. https://doi.org/10.1103/PhysRevE.64.011114.
43. Morales Martínez, J.L.; Segovia-Domínguez, I.; Quiros Rodríguez, I.; Horta-Rangel, F.A.; Sosa-Gómez, G. A Modified Multifractal Detrended Fluctuation Analysis (MFDFA) Approach for Multifractal Analysis of Precipitation. *Phys. A Stat. Mech. Its Appl.* **2021**, *565*, 125611. https://doi.org/10.1016/j.physa.2020.125611.
44. De Santis, E.; Sadeghian, A.; Rizzi, A. A Smoothing Technique for the Multifractal Analysis of a Medium Voltage Feeders Electric Current. *Int. J. Bifurc. Chaos* **2017**, *27*, 1750211. https://doi.org/10.1142/S021812741750211X.
45. Zhou, W.X. The Components of Empirical Multifractality in Financial Returns. *EPL* **2009**, *88*, 28004. https://doi.org/10.1209/0295-5075/88/28004.
46. Theiler, J.; Eubank, S.; Longtin, A.; Galdrikian, B.; Farmer, J.D. Testing for Nonlinearity in Time Series: The Method of Surrogate Data. *Phys. D Nonlinear Phenom.* **1992**, *58*, 77–94. https://doi.org/10.1016/0167-2789(92)90102-S.
47. Schreiber, T.; Schmitz, A. Improved Surrogate Data for Nonlinearity Tests. *Phys. Rev. Lett.* **1996**, *77*, 635–638. https://doi.org/10.1103/PhysRevLett.77.635.
48. Schreiber, T.; Schmitz, A. Surrogate Time Series. *Phys. D Nonlinear Phenom.* **2000**, *142*, 346–382. https://doi.org/10.1016/S0167-2789(00)00043-9.
49. Bacry, E.; Delour, J.; Muzy, J.F. Multifractal Random Walk. *Phys. Rev. E* **2001**, *64*, 026103. https://doi.org/10.1103/PhysRevE.64.026103.
50. Kantelhardt, J.W.; Koscielny-Bunde, E.; Rybski, D.; Braun, P.; Bunde, A.; Havlin, S. Long-Term Persistence and Multifractality of Precipitation and River Runoff Records. *J. Geophys. Res. Atmos.* **2006**, *111*, D01106. https://doi.org/10.1029/2005JD005881.
51. Mandelbrot, B.B. Intermittent Turbulence in Self-Similar Cascades: Divergence of High Moments and Dimension of the Carrier. *J. Fluid Mech.* **1974**, *62*, 331–358. https://doi.org/10.1017/S0022112074000711.
52. Meneveau, C.; Sreenivasan, K.R. The Multifractal Nature of Turbulent Energy Dissipation. *J. Fluid Mech.* **1991**, *224*, 429–484. https://doi.org/10.1017/S0022112091001830.
53. Ghashghaie, S.; Breymann, W.; Peinke, J.; Talkner, P.; Dodge, Y. Turbulent Cascades in Foreign Exchange Markets. *Nature* **1996**, *381*, 767–770. https://doi.org/10.1038/381767a0.
54. She, Z.S.; Leveque, E. Universal Scaling Laws in Fully Developed Turbulence. *Phys. Rev. Lett.* **1994**, *72*, 336–339. https://doi.org/10.1103/PhysRevLett.72.336.
55. Eke, A.; Hermán, P.; Bassingthwaighte, J.B.; Raymond, G.M.; Percival, D.B.; Cannon, M.; Balla, I.; Ikrényi, C. Physiological Time Series: Distinguishing Fractal Noises from Motions. *Pflügers Arch.* **2000**, *439*, 403–415. https://doi.org/10.1007/s004249900135.
56. Goldberger, A.L.; Amaral, L.A.N.; Hausdorff, J.M.; Ivanov, P.C.; Peng, C.K.; Stanley, H.E. Fractal Dynamics in Physiology: Alterations with Disease and Aging. *Proc. Natl. Acad. Sci. USA* **2002**, *99*, 2466–2472. https://doi.org/10.1073/pnas.012579499.
57. Ching, E.S.C.; Tsang, Y.K. Multifractality and Scale Invariance in Human Heartbeat Dynamics. *Phys. Rev. E* **2007**, *76*, 041910. https://doi.org/10.1103/PhysRevE.76.041910.
58. De Santis, E.; Naraei, P.; Martino, A.; Sadeghian, A.; Rizzi, A. Multifractal Characterization and Modeling of Blood Pressure Signals. *Algorithms* **2022**, *15*, 259. https://doi.org/10.3390/a15080259.
59. Muzy, J.F.; Bacry, E. Multifractal Stationary Random Measures and Multifractal Random Walks with Log Infinitely Divisible Scaling Laws. *Phys. Rev. E* **2002**, *66*, 056121. https://doi.org/10.1103/PhysRevE.66.056121.

60. Ebeling, W.; Neiman, A. Long-Range Correlations between Letters and Sentences in Texts. *Phys. A Stat. Mech. Its Appl.* **1995**, *215*, 233–241. https://doi.org/10.1016/0378-4371(95)00025-3.
61. Altmann, E.G.; Cristadoro, G.; Degli Esposti, M. On the Origin of Long-Range Correlations in Texts. *Proc. Natl. Acad. Sci. USA* **2012**, *109*, 11582–11587. https://doi.org/10.1073/pnas.1117723109.
62. Ausloos, M. Measuring Complexity with Multifractals in Texts. Translation Effects. *Chaos Solitons Fractals* **2012**, *45*, 1349–1357. https://doi.org/10.1016/j.chaos.2012.06.016.
63. Rodriguez, E.; Aguilar-Cornejo, M.; Femat, R.; Alvarez-Ramirez, J. Scale and Time Dependence of Serial Correlations in Word-Length Time Series of Written Texts. *Phys. A Stat. Mech. Its Appl.* **2014**, *414*, 378–386. https://doi.org/10.1016/j.physa.2014.07.063.
64. Drożdż, S.; Oświęcimka, P.; Kulig, A.; Kwapień, J.; Bazarnik, K.; Grabska-Gradzińska, I.; Rybicki, J.; Stanuszek, M. Quantifying Origin and Character of Long-Range Correlations in Narrative Texts. *Inf. Sci.* **2016**, *331*, 32–44. https://doi.org/10.1016/j.ins.2015.10.023.
65. Chatzigeorgiou, M.; Constantoudis, V.; Diakonos, F.K.; Karamanos, K.; Papadimitriou, C.; Kalimeri, M.; Papageorgiou, H. Multifractal Correlations in Natural Language Written Texts: Effects of Language Family and Long Word Statistics. *Phys. A Stat. Mech. Its Appl.* **2017**, *469*, 173–182. https://doi.org/10.1016/j.physa.2016.11.028.
66. De Santis, E.; De Santis, G.; Rizzi, A. Multifractal Characterization of Texts for Pattern Recognition: On the Complexity of Morphological Structures in Modern and Ancient Languages. *IEEE Trans. Pattern Anal. Mach. Intell.* **2023**, *45*, 10143–10160. https://doi.org/10.1109/TPAMI.2023.3245886.
67. Montemurro, M.A.; Degli Esposti, M. A Zipf-Preserving, Long-Range Correlated Surrogate for Written Language and Other Symbolic Sequences. *Phys. A Stat. Mech. Its Appl.* **2026**, *683*, 131227. https://doi.org/10.1016/j.physa.2025.131227.
68. Bak, P.; Tang, C.; Wiesenfeld, K. Self-Organized Criticality: An Explanation of 1/f Noise. *Phys. Rev. Lett.* **1987**, *59*, 381–384. https://doi.org/10.1103/PhysRevLett.59.381.
69. Clauset, A.; Shalizi, C.R.; Newman, M.E.J. Power-Law Distributions in Empirical Data. *SIAM Rev.* **2009**, *51*, 661–703. https://doi.org/10.1137/070710111.
70. Yu, Q.; Zhou, Z.; Yan, J.; Sun, W.; Qu, Y. Self-Organized Criticality and Multifractal Characteristics of Power-System Blackouts: A Long-Term Empirical Study of China's Power System. *Fractal Fract.* **2026**, *10*, 239. https://doi.org/10.3390/fractalfract10040239.
71. De Santis, E.; Martino, A.; Cervellini, M.; Rizzi, A. Diffusion-Limited Aggregation Signatures for Structural Text Analysis, a Case Study Across Human, LLM, Code, and Controlled Synthetic Texts. In *Proceedings of the 2026 IEEE Workshop on Complexity in Engineering (COMPENG)*; IEEE: New York, NY, USA, 2026; pp. 1–7. In press.
72. Salcedo-Sanz, S.; Álvarez-Couso, P.; Castelo-Sardina, L.; Pérez-Aracil, J. Constructing New Fractal-like Particle Aggregates Using Seeded DLA and Concentration Gradient Diffusion Approaches. *Fractal Fract.* **2026**, *10*, 68. https://doi.org/10.3390/fractalfract10010068.
73. Song, C.; Havlin, S.; Makse, H.A. Self-Similarity of Complex Networks. *Nature* **2005**, *433*, 392–395. https://doi.org/10.1038/nature03248.
74. Song, C.; Gallos, L.K.; Havlin, S.; Makse, H.A. How to Calculate the Fractal Dimension of a Complex Network: The Box Covering Algorithm. *J. Stat. Mech. Theory Exp.* **2007**, *2007*, P03006. https://doi.org/10.1088/1742-5468/2007/03/P03006.
75. Zhou, W.X.; Jiang, Z.Q.; Sornette, D. Exploring Self-Similarity of Complex Cellular Networks: The Edge-Covering Method with Simulated Annealing and Log-Periodic Sampling. *Phys. A Stat. Mech. Its Appl.* **2007**, *375*, 741–752. https://doi.org/10.1016/j.physa.2006.10.025.
76. Schneider, C.M.; Kesselring, T.A.; Andrade, José S., J.; Herrmann, H.J. Box-Covering Algorithm for Fractal Dimension of Complex Networks. *Phys. Rev. E* **2012**, *86*, 016707. https://doi.org/10.1103/PhysRevE.86.016707.
77. Pavón-Domínguez, P.; Moreno-Pulido, S. A Fixed-Mass Multifractal Approach for Unweighted Complex Networks. *Phys. A Stat. Mech. Its Appl.* **2020**, *541*, 123670. https://doi.org/10.1016/j.physa.2019.123670.
78. Pavón-Domínguez, P.; Moreno-Pulido, S. Sandbox Fixed-Mass Algorithm for Multifractal Unweighted Complex Networks. *Chaos Solitons Fractals* **2022**, *156*, 111836. https://doi.org/10.1016/j.chaos.2022.111836.
79. Moreno-Pulido, S.; Pavón-Domínguez, P.; Burgos-Pintos, P. Temporal Evolution of Multifractality in the Madrid Metro Subway Network. *Chaos Solitons Fractals* **2021**, *142*, 110370. https://doi.org/10.1016/j.chaos.2020.110370.
80. Plocoste, T.; Carmona-Cabezas, R.; Jiménez-Hornero, F.J.; Gutiérrez de Ravé, E. Background PM10 Atmosphere: In the Seek of a Multifractal Characterization Using Complex Networks. *J. Aerosol Sci.* **2021**, *155*, 105777. https://doi.org/10.1016/j.jaerosci.2021.105777.
81. Díaz-Jiménez, M.; Pavón-Domínguez, P.; Ruiz, P.; Moreno-Pulido, S. Exploring Multifractal Geometry in Directed Complex Networks. *Phys. A Stat. Mech. Its Appl.* **2026**, *690*, 131478. https://doi.org/10.1016/j.physa.2026.131478.
82. Krioukov, D.; Papadopoulos, F.; Kitsak, M.; Vahdat, A.; Boguñá, M. Hyperbolic Geometry of Complex Networks. *Phys. Rev. E* **2010**, *82*, 036106. https://doi.org/10.1103/PhysRevE.82.036106.
83. Ren, H.; Yu, Z.G.; Liu, J.L. Multifractal Analysis of Structural Perturbation Time Series in Hyperbolic Growing Networks. *Chaos Solitons Fractals* **2026**, *208*, 118331. https://doi.org/10.1016/j.chaos.2026.118331.

84. Zhang, Y.; Zhou, W.; Yuan, S. Multifractal Analysis and Relevance Vector Machine-Based Automatic Seizure Detection in Intracranial EEG. *Int. J. Neural Syst.* **2015**, *25*, 1550020. https://doi.org/10.1142/S0129065715500203.
85. França, L.G.S.; Vivas Miranda, J.G.; Leite, M. Fractal and Multifractal Properties of Electrographic Recordings of Human Brain Activity: Toward Its Use as a Signal Feature for Machine Learning in Clinical Applications. *Front. Physiol.* **2018**, *9*, 1767. https://doi.org/10.3389/fphys.2018.01767.
86. Wang, F.; Wang, L.; Zou, R.B. Multifractal Detrended Moving Average Analysis for Texture Representation. *Chaos* **2014**, *24*, 033127. https://doi.org/10.1063/1.4894763.
87. Shi, W.; Zou, R.B.; Wang, F.; Su, L. A New Image Segmentation Method Based on Multifractal Detrended Moving Average Analysis. *Phys. A Stat. Mech. Its Appl.* **2015**, *432*, 197–205. https://doi.org/10.1016/j.physa.2015.03.058.
88. Wang, X.; Li, Y.; Han, G.; Wang, F. Adaptive Multifractal Correlation Analyses and Its Variants for Classification of Complex Image. *Phys. A Stat. Mech. Its Appl.* **2026**, *695*, 131624. https://doi.org/10.1016/j.physa.2026.131624.
89. De Santis, E.; Martino, A.; Ronci, F.; Rizzi, A. LSTM in Recursive Feedback Loops: A Study on Textual Evolution and Complexity. In *Proceedings of the 2025 International Joint Conference on Neural Networks (IJCNN)*; IEEE: New York, NY, USA, 2025; pp. 1–10. https://doi.org/10.1109/IJCNN64981.2025.11227357.
90. De Santis, E.; Martino, A.; Rizzi, A. Beyond Perplexity: A Multi-Faceted Analysis of a Novel Densely Connected Transformer. *Appl. Sci.* **2026**, *16*, 2721. https://doi.org/10.3390/app16062721.
91. Engel, A.; Van den Broeck, C. *Statistical Mechanics of Learning*; Cambridge University Press: Cambridge, UK, 2001. https://doi.org/10.1017/CBO9781139164542.
92. Facco, E.; d'Errico, M.; Rodriguez, A.; Laio, A. Estimating the Intrinsic Dimension of Datasets by a Minimal Neighborhood Information. *Sci. Rep.* **2017**, *7*, 12140. https://doi.org/10.1038/s41598-017-11873-y.
93. Gong, S.; Boddeti, V.N.; Jain, A.K. On the Intrinsic Dimensionality of Image Representations. In *Proceedings of the IEEE/CVF Conference on Computer Vision and Pattern Recognition*; IEEE: New York, NY, USA, 2019; pp. 3987–3996. https://doi.org/10.1109/CVPR.2019.00411.
94. Chung, S.; Lee, D.D.; Sompolinsky, H. Classification and Geometry of General Perceptual Manifolds. *Phys. Rev. X* **2018**, *8*, 031003. https://doi.org/10.1103/PhysRevX.8.031003.
95. Cohen, U.; Chung, S.; Lee, D.D.; Sompolinsky, H. Separability and Geometry of Object Manifolds in Deep Neural Networks. *Nat. Commun.* **2020**, *11*, 746. https://doi.org/10.1038/s41467-020-14578-5.
96. Ansuini, A.; Laio, A.; Macke, J.H.; Zoccolan, D. Intrinsic Dimension of Data Representations in Deep Neural Networks. *Adv. Neural Inf. Process. Syst.* **2019**, *32*, 6111–6122.
97. Valeriani, L.; Doimo, D.; Cuturello, F.; Laio, A.; Ansuini, A.; Cazzaniga, A. The Geometry of Hidden Representations of Large Transformer Models. *Adv. Neural Inf. Process. Syst.* **2023**, *36*, 51234–51252. https://doi.org/10.52202/075280-2230.
98. Doimo, D.; Serra, A.; Ansuini, A.; Cazzaniga, A. The Representation Landscape of Few-Shot Learning and Fine-Tuning in Large Language Models. *Adv. Neural Inf. Process. Syst.* **2024**, *37*, 18122–18165. https://doi.org/10.52202/079017-0576.
99. Schulte, R.; Rügamer, D. Rethinking Intrinsic Dimension Estimation in Neural Representations. In *Proceedings of the 29th International Conference on Artificial Intelligence and Statistics*; Proceedings of Machine Learning Research; PMLR: London, UK, 2026; Volume 300, pp. 10–18.


**Disclaimer/Publisher's Note:** The statements, opinions and data contained in all publications are solely those of the individual author(s) and contributor(s) and not of MDPI and/or the editor(s). MDPI and/or the editor(s) disclaim responsibility for any injury to people or property resulting from any ideas, methods, instructions or products referred to in the content.